MODELING OF AMMONIA SYNTHESIS REACTION IN MEMBRANE-INTEGRATED MICROREACTORS FOR SMALL-SCALE APPLICATIONS

by

Damla Sıvacı

B.S., Chemical Engineering, Istanbul Technical University, 2022

Submitted to the Institute for Graduate Studies in
Science and Engineering in partial fulfillment of the
requirements for the degree of
Master of Science

Graduate Program in Chemical Engineering
Boğaziçi University
2024

To my family and my love

ACKNOWLEDGEMENTS

I would like to extend my gratitude to Prof. Dr. Ahmet Kerim Avcı, who provided all kinds of support throughout the thesis process, regularly monitored my work, and guided me with his extensive knowledge. I am greatly honored to have taken the first steps of my career under his supervision. Additionally, I am grateful for the opportunity to present my work at ISCRE28 in Finland.

I would also like to express my gratitude to Prof. Dr. Ramazan Yıldırım and Prof. Dr. Ayşe Nilgün Akın for generously investing their time in reading and evaluating my research.

I would like to thank every member of KB 404; Necdet Semih Altınsoy, Mert Özden, Emre Küçük, Orhun Harmancılar, Gözde Kara and İrem Taşpınar.

I would like to express my love for my family. I want to thank my mother and father, Gülbahar Sıvacı and Salih Sıvacı, for being more than just parents, for their countless sacrifices which I may not even be aware of, for bringing me to where I am today and providing me with a beautiful life. To my brother, Umut Sıvacı, who is not only a brother but also my closest friend and greatest supporter, I want to express my endless gratitude for all the love and support from my entire family. They have been there for me in every success and setback, always supporting me, doing everything they could to help me succeed and find happiness, and they have guided me to reach this point in my life and career. I am incredibly lucky to have such a family. Many thanks to this wonderful family.

I am grateful to my beloved, my closest friend, dear Mustafa Furkan Ayan, with whom I have grown up, who has been by my side at every moment, with whom we have overcome challenges together, shared my happiness and sadness, and who desires my success at least as much as I do. Thank you so much for this wonderful friendship, deep love, and everything.

I sincerely thank my colleagues and dear sisters Dilara Küçükay and Melis Özkan, whom I befriended during my undergraduate years at Istanbul Technical University, and Pelin Gümüş, with whom I lived in the ITU dorms and who became more than a sister to me, for their unwavering support and beautiful friendship, and always being there for me.

Finally, I would like to express my gratitude to TUBITAK BIDEB 2210/A National MSc/MA Scholarship Program for providing me with a scholarship for my M.Sc. degree.

ABSTRACT

MODELING OF AMMONIA SYNTHESIS REACTION IN MEMBRANE-INTEGRATED MICROREACTORS FOR SMALL-SCALE APPLICATIONS

The cascade of packed–bed reactors (PBRs) and microchannel membrane heat exchangers (micro–HExs) is modeled using ANSYS and MATLAB under 2D and 1D, non-isothermal, steady-state conditions. Permeate and reaction channels are physically segregated by layers of $ZnCl_2$-immobilized molten salt (IMS) membrane that is selective for NH_3 transport. Each Fe-based catalyst packed adiabatic PBR effluent, composed of H_2-N_2-NH_3 mixture, is supplied into the reaction channels while N_2 is supplied in the permeate channels as the sweep gas that regulates the inlet temperature of the PBR. Modeling considers the conservation of mass, momentum, and energy in the PBR and the micro-HExs. Membrane separation is modeled by Fick's' law. Output of the reaction channel is dosed to the next PBR where synthesis takes place. Due to the laminar flow conditions in the micro-HEx units, heat transfer and separation are solved simultaneously in ANSYS (v. 19.2) for both co- and counter-current flow. The solutions are compared with MATLAB, which is also used in simulating adiabatic catalytic reaction in the PBRs by a 1D pseudohomogeneus model. Upon validating the similarity of two models, MATLAB is used, then PBR and micro-HEx units are integrated under a single code. It is observed that the counter-current mode yielded better results. Later, two different configurations are designed to improve the system. The first involves adding a fresh nitrogen flow at 573K to the output of the reaction channel. In this arrangement, the temperature profile is observed to be as desired. Additionally, there is a significant increase in the converted nitrogen ratio. The other configuration involves feeding the outlet of the sweep channel into the next one. This prevents the issue of additional fresh N_2 feed and helps increase the fraction of ammonia in the sweep channel, thereby facilitating the necessary conditions for obtaining pure ammonia in the later stages. As a result, a system consisting of 5 units operating in a counter-current mode with additional N_2 feed and interconnected heat exchangers is optimal based on these calculations.

OZET

MEMBRAN ENTEGRE EDİLMİŞ MİKROREAKTÖRLERDE KÜÇÜK ÖLÇEKLİ UYGULAMALAR İÇİN AMONYAK SENTEZİ REAKSİYONUNUN MODELLENMESİ

Dolgu yataklı reaktörlerden (PBR) ve membranlı mikrokanal ısı değiştiricilerden (micro-HEx) oluşan kaskad sistem, ANSYS ve MATLAB kullanılarak 2D ve 1D, non-izotermal, durağan durum koşulları altında modellenmiştir. Süpürme ve reaksiyon kanalları, NH_3 geçişine seçici olan $ZnCl_2$-immobilize erimiş tuz membran katmanlarıyla fiziksel olarak ayrılmıştır. Fe-bazlı katalizörle dolu adiabatik PBR'nin çıkışı, H_2-N_2-NH_3 karışımından oluşur ve bu akım reaksiyon kanallarına, süpürme gazı olarak N_2, permeat kanallarına beslenir ve PBR giriş sıcaklığını düzenler. Modellemede PBR ve micro-HEx'larda kütle, momentum ve enerji korunumu göz önünde bulundurulmuştur. Membran ayrımı Fick yasası ile modellenmiştir. Reaksiyon kanalının çıkışı, sentezin gerçekleştiği bir sonraki PBR'ye dozlanır. Mikro-HEx ünitelerindeki laminar akış koşulları nedeniyle, ısı transferi ve ayırma hem ko- hem de karşı-akım akışları için ANSYS (v.19.2)'de eş zamanlı olarak çözülmüştür. Çözümler MATLAB ile karşılaştırılmıştır; MATLAB ayrıca PBR'lerde adiabatik katalitik reaksiyonu 1D psödohomojen model ile simüle etmek için kullanılır. İki modelin benzerliği doğrulandıktan sonra, MATLAB platformu kullanılarak PBR ve micro-HEx üniteleri tek bir kod altında entegre edilmiştir. Karşı-akım modunun daha iyi sonuçlar verdiği gözlemlenmiştir. Daha sonra, sistemi iyileştirmek için iki farklı konfigürasyon tasarlanmıştır. İlk konfigürasyon, reaksiyon kanalının çıkışına 573K'de taze azot akışı eklemeyi içerir. Bu düzenlemede, sıcaklık profili istenildiği gibi gözlemlenmiştir. Ayrıca, dönüştürülen azot oranında önemli bir artış olmuştur. Diğer konfigürasyon ise süpürme kanalının çıkışını bir sonraki ısı değiştiriciye beslemeyi içerir. Bu, ekstra taze N_2 beslemesi sorununu önler ve süpürme kanalındaki amonyak fraksiyonunu artırarak sonraki aşamada saf amonyak elde etmek için gerekli koşulu sağlamaya yardımcı olur. Bu hesaplamalara göre, ek N_2 beslemesi ve birbirine bağlı ısı değiştiriciler ile çalışan, karşı-akım modunda 5 üniteden oluşan sistem optimaldir.

TABLE OF CONTENTS

LIST OF FIGURES

LIST OF TABLES

LIST OF SYMBOLS

A	Arrhenius constant
A_c	Cross sectional area
c_p	Heat capacity
d_p	Particle diameter
d_{pore}	Pore diameter
E_a	Activation energy
F_i	Molar flow rate
g	Constant
H	Enthalpy
J	Flux
K	Reaction equilibrium constant
k	Constant
k_A	Forward rate constant
k_B	Backward rate constant
$Perm_{NH_3}$	Permeability of ammonia
P_i	Partial pressure
r	Reaction rate
r_s	Adsorption rate of N_2
t_{mem}	Thickness of membrane
W	Catalyst weight
θ_N	Coverage by N_2 adsorption
ε_{bed}	Bed porosity
τ_{cat}	Tortuosity

LIST OF ACRONYMS/ABBREVIATIONS

1D	One Dimensional
2D	Two Dimensional
CCS	Carbon Capture and Storage
CCUS	Carbon Capture Utilization and Storage
CO_2	Carbon Dioxide
CSMR	Steam Methane Reforming
H_2	Hidrogen
LOHC	Liquid Organic Hydrogen Carrier
Mt	Million Ton
N_2	Nitrogen
NH_3	Ammonia
PEM	Proton Exchange Membrane
PV	Photovoltaic

1. INTRODUCTION

The increasing reliance on fossil fuels has triggered substantial climate change and raised significant health concerns within communities globally. Addressing these pressing issues necessitates a widespread transition towards clean energy sources. These sustainable energy alternatives not only offer a pathway to combat climate change but also carry minimal adverse effects on the environment [1]. In recent times, there has been a significant increase in interest towards renewable energy sources as a means to drive global energy transitions towards low-carbon or carbon-free resources. Solar and wind power are key solutions for large-scale electricity generation. While battery storage can tackle certain energy challenges, its application is limited in large-scale settings. Wind power stands out as the most prominent commercial renewable energy globally, with solar energy also gaining widespread attention. Solar power is considered a vital renewable energy source, with well-established applications like photovoltaics, solar heating/cooling, and solar thermal electricity. However, both solar and wind energy are reliant on environmental conditions, geographical locations, and seasonal variations [2].

Utilizing a range of energy storage methods including thermal, mechanical, electrochemical, and chemical systems is crucial for enhancing and maintaining the accessibility of sustainable energy sources. An impactful strategy in this area involves integrating green hydrogen with renewable energy sources [1]. Green hydrogen is produced from renewable sources like wind and solar power, contrasting with gray hydrogen derived from fossil fuels with associated CO_2 emissions. Hydrogen can also be generated through steam methane reforming (SMR) by utilizing hydrocarbon fuels as feedstock along with carbon capture and storage (CCS). Various other types of hydrogen, such as brown hydrogen from coal gasification, turquoise hydrogen from methane pyrolysis, and pink hydrogen from water electrolysis using nuclear-powered electricity, have been explored in hydrogen production processes [2].

Hydrogen energy, characterized by its green, low-carbon nature, widespread availability, and high calorific value, serves as a crucial secondary energy source. With zero carbon emissions and versatile applications, hydrogen energy holds significant value in advancing low-carbon development within renewable energy systems. Unlike pumped storage and electrochemical storage, hydrogen energy is environmentally friendly and unaffected by external conditions. Hydrogen energy can be derived from various sources, including fossil fuels, industrial by-products, and water electrolysis. The global consensus increasingly supports the production of hydrogen energy from renewable sources, underscoring its importance in the transition towards sustainable energy systems [3].

Global hydrogen demand saw a 5% rise in 2021, indicating a rebound in economic activities in traditional sectors following pandemic-related disruptions. Total global hydrogen demand surpassed 94 million tonnes (Mt) in 2021, up 5% from the previous year and compared to 91 Mt in 2019 (pre-pandemic levels) as can be observed from Figure 1.1. The surge primarily stemmed from increased usage in traditional sectors, notably chemicals with a nearly 3 Mt increase and refining with approximately 2 Mt rise from 2020. China leads as the largest consumer with a 5% rise in demand in 2021, reaching around 28 Mt H_2. The United States and the Middle East follow closely as the second and third-largest consumers, each consuming about 12 Mt H_2 in 2021, marking an 8% and 11% increase, respectively, from 2020. Europe stands as the fourth-largest consumer, maintaining a demand of over 8 Mt H_2 in 2021, similar to 2020 levels. India ranks next with an 8 Mt H_2 demand, up 7% from the previous year due to economic recovery, notably in refining and steel production sectors that faced significant impacts from the 2020 pandemic [4].

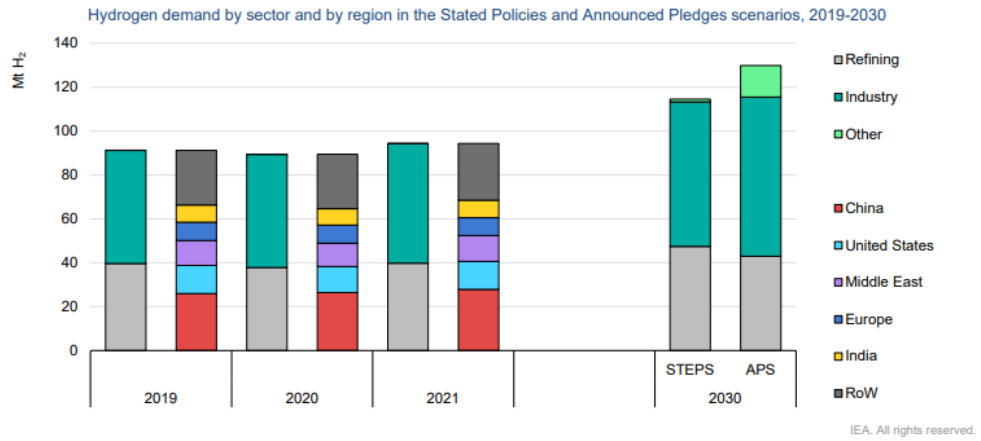

Figure 1.1. Global hydrogen demand according to countries and sectors (STEPS = Stated Policies Scenario; APS = Announced Pledges Scenario. Other includes transport, buildings, power generation sectors and production of hydrogen-derived fuels and hydrogen blending).

Hydrogen utilization faces problems related to effective storage and transportation infrastructure [1]. Conventional physical storage methods like compressed, liquid, and adsorbed hydrogen, while common, possess drawbacks such as low storage density, high expenses, and safety concerns. Recent years have witnessed the emergence of new hydrogen storage technologies like underground hydrogen storage. This method offers superior efficiency, safety, and cost-effectiveness in hydrogen energy storage, showcasing potential for wider adoption within renewable energy systems [3].

Liquid organic hydrogen carrier (LOHC) systems have gained significant attention for hydrogen storage and transportation. Advanced catalysts have been created for storing hydrogen within LOHC. Various choices exist for producing liquid energy carriers, including liquefied hydrogen, LOHCs, ammonia, and products from CO_2 reduction. Among these options, the CO_2 reduction and hydrogen liquefaction processes are the most expensive, necessitating consideration alongside safety and practicality factors. Ammonia is increasingly recognized as a promising clean energy source for future global renewable fuel alternatives [2].

With a significant gravimetric hydrogen content of 17.6 wt %, a notable volumetric hydrogen energy density of 10.7 kg H_2/100 L, and its ease of liquefaction for storage, handling, and transportation, NH_3 is being evaluated as a potential fuel and hydrogen carrier [5]. Ammonia can readily be liquefied at room temperature under a moderate pressure of 10 bar or at atmospheric pressure through cooling to -33°C. Despite its advantages such as a limited flammability range and high power-to-fuel efficiency, ammonia is hindered by its toxicity, substantial NO_x and NH_3 emissions, and relatively low reactivity as a fuel [2].

In Table 1.1, a comparison of thermal properties and combustion characteristics between ammonia and other common fuels is detailed. Notably, hydrogen gas liquefaction necessitates an extremely low temperature of -252.9°C, leading to the need for expensive storage equipment. Storing hydrogen at ambient temperatures requires very high pressure, resulting in elevated costs and energy demands for storage and transportation. Conversely, ammonia emerges as a promising carrier for higher hydrogen energy due to its superior volumetric energy density compared to liquid hydrogen, positioning it as a highly attractive hydrogen energy carrier [2]. Ammonia stands out with a superior volumetric energy density compared to liquid hydrogen, establishing it as a highly appealing hydrogen energy carrier. As a carbon-free hydrogen energy carrier, ammonia has the capacity to store significant amounts of renewable electricity. Its utilization enables the provision of clean and reliable renewable energy for a variety of applications, both stationary and mobile. Furthermore, ammonia serves as an energy vector, offering an alternative carbon-free fuel source that can be directly fed into internal combustion engines. Beyond its carbon-free attributes, ammonia can store more hydrogen energy per unit volume at a reduced cost compared to other alternative energy carriers [6].

Table 1.1. Comparison of the common fuels.

Fuel	NH_3	H_2	CH_4	C_3H_8
Boiling temperature at 1 atm (°C)	−33.4	−253	−161	−42.1
Condensation pressure at 25 °C (atm)	9.9	N/A	N/A	9.4
Low heating value, LHV (MJ/kg)	18.6	120	50	46.4
Flammability limit (equivalence ratio)	0.63–1.4	0.1–7.1	0.5–1.7	0.51–2.5
Adiabatic flame temperature (°C)	1800	2110	1950	2000
Maximum laminar burning velocity (m/s)	0.07	2.91	0.37	0.43
Minimum Autoignition temperature (°C)	650	520	630	450

Ammonia, with an annual production capacity exceeding 200 million tons, plays a vital role in sustaining life and the global chemical industry. Around 80% of industrial ammonia is dedicated to fertilizer production for agricultural purposes, with the remaining 20% employed in the manufacturing of explosives, pharmaceuticals, refrigerants, and cleaning products [5].

Figure 1.2 illustrates the global production of ammonia by each country. China accounts for approximately 30% of the world's ammonia production, contributing to 45% of the CO_2 emissions associated with this production. Other regions such as the Middle East, the United States, Russia, the European Union, India, and various other areas now produce between 8% and 10% of the world's ammonia each [7].

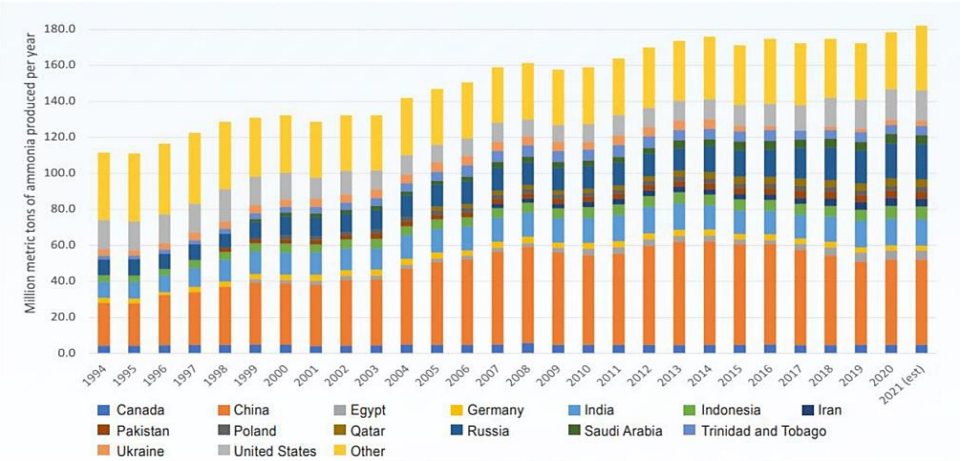

Figure 1.2. Global production of ammonia.

The global focus on utilizing ammonia as both a hydrogen energy carrier and fertilizer for agriculture is expected to boost annual ammonia production. According to projections, Figure 1.3 illustrates the increase in ammonia output relative to its usage. With population expansion and global trends in mind, ammonia production is anticipated to surge by 40% by 2050. Prior to worldwide energy regulations, it is estimated that CO_2 emissions from ammonia production processes will hit around 3% by 2030 [7].

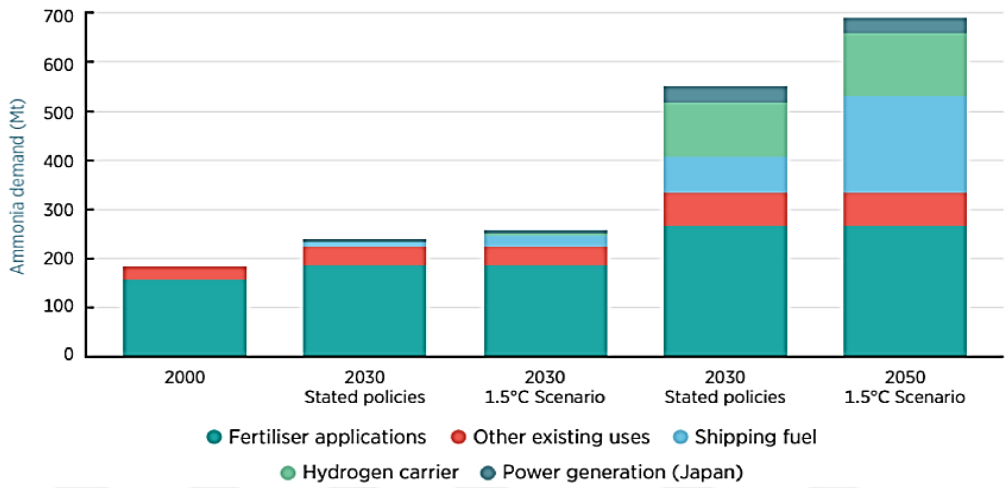

Figure 1.3. Various usage areas of ammonia.

In 1908, the German chemist Fritz Haber devised a technique for synthesizing ammonia from H_2 and N_2 at high pressure and temperature, incorporating recycling. This method was later industrialized by Carl Bosch, leading to the establishment of the first ammonia synthesis plant in 1911, commonly referred to as the Haber-Bosch process [8].

Presently, the Haber-Bosch process is employed in large-scale facilities for ammonia production, accounting for approximately 1.8% of the world's yearly energy consumption (with over 80% of the energy utilized in steam methane reforming). Considered one of the "big four" industrial processes alongside cement, steel, and ethylene, it stands out as the largest emitter of carbon dioxide among chemical processes, releasing roughly 500 million tons annually. Efforts to develop carbon-free ammonia production could significantly reshape industrial practices, focusing on enabling ammonia synthesis from green hydrogen while leveraging renewable energy sources to reduce carbon emissions [9].

The ammonia synthesis pathway can be visualized in Figure 1.4, with the first pathway relying on fossil fuels as a Haber-Bosch process feedstock. Reports indicate that NH_3 synthesis using fossil fuels as a feedstock results in the highest CO_2 emissions. The NH_3 synthesis process pathway utilizing fossil fuels as a feedstock is termed "Gray Ammonia" due to its high carbon emissions. In contrast, efforts to mitigate CO_2 emissions have led to the development of "Blue Ammonia," where carbon capture utilization and storage (CCUS) techniques are applied to reduce the environmental impact of NH_3 synthesis. Hydrogen can be produced through water electrolysis using renewable electricity from sources like wind or solar PV cells for NH_3 synthesis. Pure hydrogen can be derived from different water electrolyzer types, such as alkaline and proton exchange membrane (PEM), with renewable energy sources. Consequently, this NH_3 synthesis route is termed "Green Ammonia," where the use of renewable electricity significantly lowers carbon emissions, almost to zero. The green ammonia production process is crucial in diminishing carbon emissions from hydrogen production using fossil fuels when compared to gray and blue ammonia production methods [6].

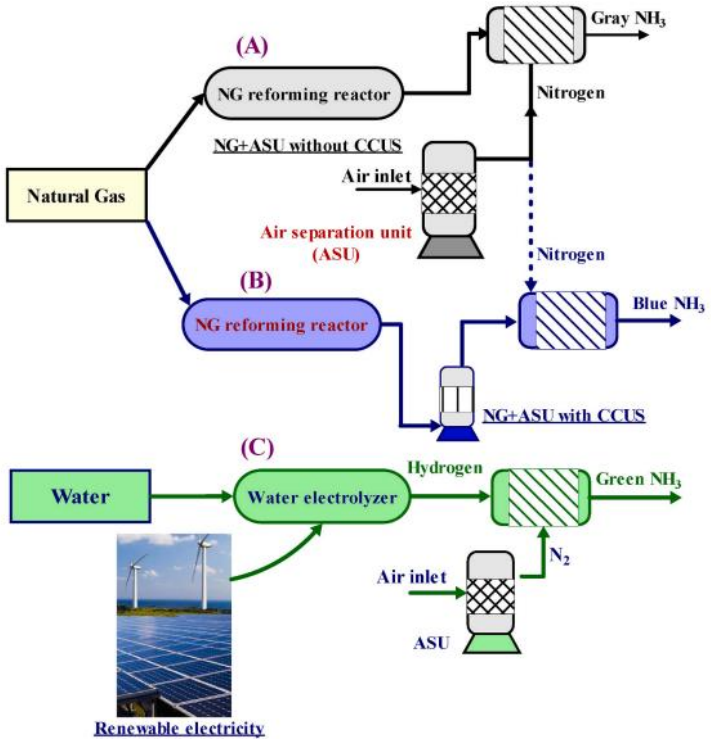

Figure 1.4. Ammonia synthesis processes.

The Haber-Bosch process for ammonia synthesis represents a sustainable, carbon-free production method by replacing methane or fossil fuels with renewable hydrogen production technologies like water electrolysis. Comparing key renewable energy inputs, various technological parameters, including energy efficiency and responsiveness, are impacted by the electric process. Water electrolysis has begun facilitating renewable hydrogen production with superior heat integration compared to the SMR process. However, challenges persist, notably in material costs and durability of electrolyzers. While efficiencies are on the rise, these systems remain costly in contrast to fossil fuel-based hydrogen production. Further advancement in electrolyzer technology is essential to reduce energy consumption, operational expenses, and enhance durability [2].

The following describes how hydrogen and nitrogen react to create ammonia

$$3H_2 + N_2 \leftrightarrow 2NH_3 \quad \Delta Hr° = -91.8 \text{ kJ mol}^{-1}. \tag{1.1}$$

The Haber-Bosch process is exothermic, favoring ammonia production under high pressure and low temperature equilibrium conditions. Despite the potential for near 100% ammonia equilibrium concentration at low temperatures and high pressures, the synthesis rate is slow for industrial purposes. Hence, the process is conducted at elevated pressures and temperatures, leading to altered equilibrium conditions, slower production rates, and ammonia breakdown. Catalyst surface reactions between nitrogen and hydrogen play a crucial role in catalytic ammonia production, involving chemisorption where reactants bond chemically with the catalyst surface, differing from physisorption where a physical bond is formed. In catalyst theory, the focus lies on how reactants behave during the adsorption phase. The quest for new catalysts is pivotal in achieving green ammonia production through an efficient Haber-Bosch process [8]. Developing highly active catalysts poses a significant challenge in enhancing the ammonia synthesis process to minimize waste and mitigate environmental impacts. Bosch's assistant was tasked with finding more reliable and efficient catalysts. By exploring metal nitrides, they delved into the fixation of nitrogen from the air. Their research revealed that certain metals influenced catalytic activity, which could be enhanced by introducing promoters. Iron-based catalysts, widely recognized for their efficiency, have been utilized in ammonia synthesis since 1910. Moreover, Ru-based catalysts are being investigated for their high activity and thermal stability for potential use in the next generation of ammonia synthesis [7].

2. LITERATURE SURVEY

2.1. Catalysts for Ammonia Synthesis

A critical component in the ammonia synthesis cycle is the catalyst, which plays a pivotal role. The catalyst's efficiency is a key indicator of the operational temperature of the reactor. The durability of the catalyst, influenced by its resilience against chemical conditions such as impurities and physical conditions like extreme temperatures, is a crucial factor in assessing the duration of the process before a catalyst replacement becomes necessary. Catalysts that are capable of withstanding and enabling rapid startup and flexible operation will be crucial for managing the intermittent nature of renewable energy sources. Consequently, catalysts that exhibit high activity even at low operating conditions such as reduced pressure and temperature and that can tolerate impurities well, are essential for the agile operation of production facilities. These characteristics are particularly important for the production of green ammonia. From this perspective, the quest for improved catalysts that can efficiently synthesize ammonia through the Haber-Bosch process is vital for the realization of green ammonia production. In 1920s, it was established that the strength of nitrogen binding is a critical factor in determining ammonia synthesis activity. Electronic promoters play a significant role in altering the activity by affecting the barrier to breaking the triple N≡N bond. A "volcano curve" can be seen in Figure 2.1 was introduced, where nitrogen binding strength serves as a key indicator for the rate of ammonia synthesis. Catalysts that bind nitrogen too strongly (left side of the curve) may have issues with nitrogen dissociation, while those binding too weakly (right side) face barriers to nitrogen dissociation. Optimal performance is achieved at an intermediate nitrogen binding strength. Osmium and ruthenium exhibit higher activity than iron among metal catalysts. Bimetallic catalysts like CoMo nitrides have shown performance comparable to ruthenium. Although ruthenium has been used in industrial settings, its high cost has led to a shift towards the latest generation of iron-based catalysts. Osmium, however, is toxic and unsuitable for use. Current research focuses on developing catalysts that efficiently break the N≡N bond, with hydrogenation of N as the crucial step on the catalyst surface [10].

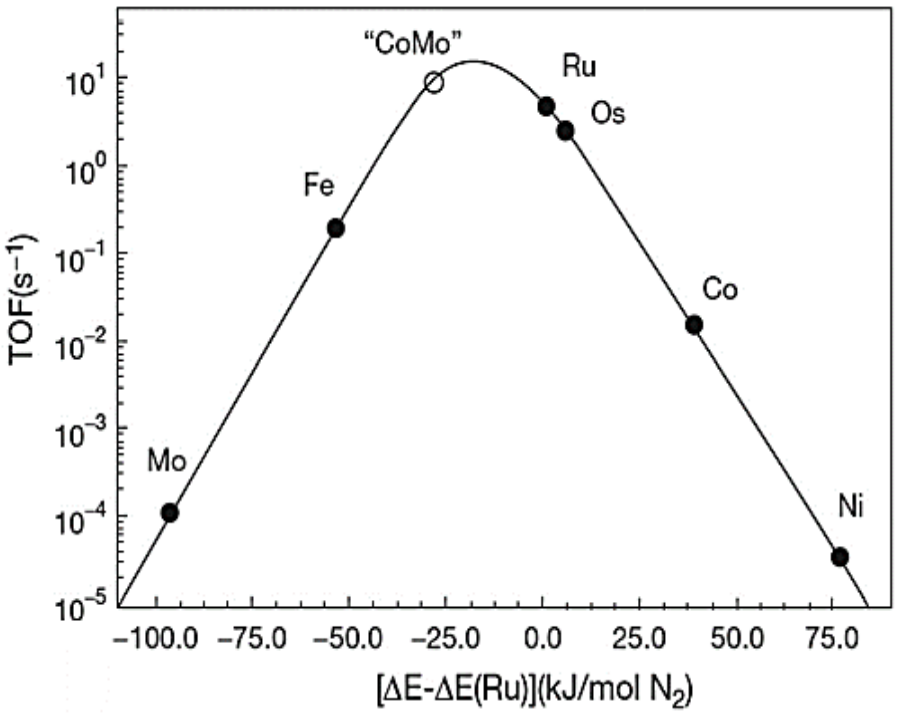

Figure 2.1. The turnover frequencies for ammonia synthesis based on the nitrogen adsorption energy (at 400°C, 50 bar, H_2/N_2 = 3:1, and 5% NH_3).

The most commonly utilized catalyst in the synthesis of ammonia is an iron-based catalyst that has been enhanced with multiple promoters. This catalyst includes a combination of alumina (Al_2O_3), magnesium oxide (MgO), and silicon dioxide (SiO_2), which serve to provide mechanical strength and act as structural promoters. Additionally, it contains electronic promoters such as calcium oxide (CaO) and potassium oxide (K_2O). These promoters help to improve the performance and efficiency of the catalyst. Iron-based catalysts of this type are known for their durability and typically have a lifespan of at least ten years under normal operating conditions. This longevity makes them a reliable choice for industrial ammonia production processes. The diagram of the catalysts used it is given in Figure 2.2 [8].

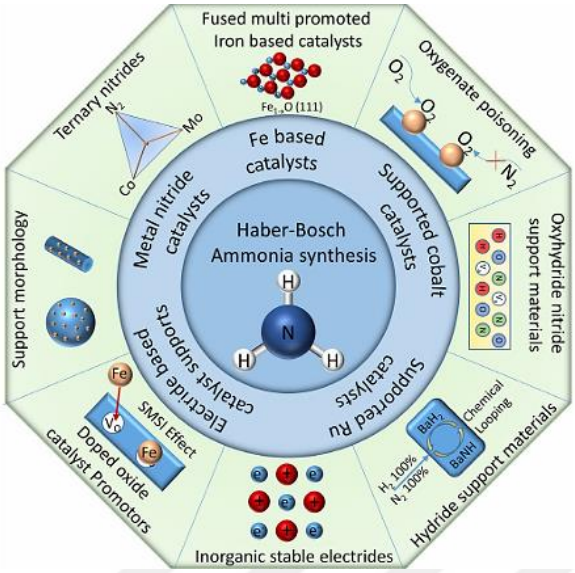

Figure 2.2. Visual representation detailing methods to enhance Haber-Bosch ammonia production.

2.1.1. Iron Catalysts

Among the various catalysts used in the production of ammonia, fused-iron catalysts have been the most extensively studied and widely adopted. The creation of the fused iron catalyst for ammonia synthesis established the groundwork for the advancement of heterogeneous catalysis as it is known today. For over 90 years, the history of efforts to enhance the properties of the iron catalyst has not led to a significant breakthrough [11].

These catalysts can be derived from three different iron oxides: Fe_2O_3 (hematite), Fe_3O_4 (magnetite), and $Fe_{1-x}O$ (wüstite). Of these, magnetite-based catalysts are the ones most frequently employed in commercial ammonia synthesis. The initial catalysts for ammonia synthesis were made from magnetite, as it was believed to possess the highest level of activity. Consequently, the promoters added to magnetite catalysts to enhance their catalytic activity have been a focal point of catalyst research throughout the last century [8].

The primary components of a traditional iron catalyst based on magnetite include iron oxide Fe_3O_4 and metal oxide promoters, commonly aluminum oxide (Al_2O_3), calcium oxide (CaO), and potassium oxide (K_2O). The catalyst's effectiveness in the ammonia synthesis reaction has historically been influenced by the composition and types of promoters. The ratio of iron ions Fe^{2+}/Fe^{3+} was not thoroughly considered in relation to the classic volcano-shaped curve that describes how catalytic activity depends on this ratio, denoted as R. As per this curve, catalysts with an R-value approximating 0.5, mirroring the iron ion ratio in natural magnetite, exhibit optimal activity [11].

Aika and Ozaki employed a 2.2 wt% promoter to investigate the application of Al_2O_3 promoter with an iron catalyst. While they confirmed role of Al_2O_3 as a sintering inhibitor, they did not observe an increase in yield compared to their unpromoted catalyst test [8].

Ommen, Bolink, Prasad and Mars conducted extensive research on potassium promoters. Initially, tests with KOH as a promoter indicated a decrease in activity due to potassium remaining in the hydroxide state during synthesis conditions and forming a robust bond with the iron surface. Subsequent investigations demonstrated that potassium promoters exhibited limited performance under low pressure conditions, but significantly enhanced activity was observed with increased pressure [8].

Research into ammonia synthesis catalysts has not been limited to those made of pure iron; iron alloys have also been explored for this purpose. In a study conducted by Taylor, Smith, Dowden, Kemball and Whan, the potential of iron alloy catalysts investigated. The results of their research showed that both the iron-cobalt and iron-nickel catalysts demonstrated superior activity compared to the catalyst composed solely of iron. Despite the enhanced performance, the higher cost of nickel relative to iron could present a significant barrier to the commercial viability of nickel-containing catalysts [8].

Additionally, it has been observed that the surface structure of the crystals in iron-based catalysts plays a role in determining their activity. The study by Spencer, Schoonmaker and Somorjai investigated the influence of surface structure on the catalytic performance of single-crystal iron catalysts in ammonia synthesis. They examined three different crystal planes; the (110) plane, which is densely packed and has six exposed coordinated atoms, the (100) plane, which is less closely packed and has four exposed coordinated atoms, the (111) plane, which is the most open and has a combination of four and seven exposed coordinated atoms. The findings from this research indicated that among the three planes studied, the (111) crystal surface showed the highest rate of ammonia synthesis when compared to the (100) and (110) planes. This suggests that the arrangement of atoms on the surface of the catalyst plays a significant role in determining its efficiency for ammonia production. The more open structure of the (111) plane may provide a more favorable environment for the reaction to occur, either by facilitating the adsorption of reactants or by allowing for easier desorption of the product ammonia, thus enhancing the overall catalytic activity [8].

Wang, Chang, Gao, Guo, Wu, He and Chen recently presented findings highlighting how lithium hydride, when combined with iron at a 5 to 1 ratio, significantly boosts the activity of iron and metal hydrides in generating ammonia. In contrast to traditional catalysts where iron is predominant with minor promoters, this catalyst, with only 58% iron content, shows substantial activity at lower temperatures. Nonetheless, the intricate manufacturing process and vulnerability to air and moisture could hinder the practical use of these hydride catalysts [8].

Gao and colleagues have conducted further research on hydride catalysts employing iron. Their study utilized a 20% Fe-BaH_2 catalyst, which exhibited good activity at moderate temperatures despite the low iron content. Unlike the traditional method of supplying hydrogen and nitrogen in a 3 to 1 ratio, this research introduced a novel approach where pure nitrogen and pure hydrogen feeds were alternated to create a synthesis gas loop. In this chemical looping process, the hydride support undergoes nitridation through pure nitrogen flow, followed by hydrogenation to produce ammonia.

Implementing this technique resulted in a 4.5 times increase in activity of the 20% Fe-BaH_2 catalyst at a temperature 50°C lower. Moreover, recent studies involving an electric field applied to a Fe catalyst supported on CeO_2 demonstrated exceptional activity at an extremely low temperature of 100°C. The 7% Fe-CeO_2 catalyst with low iron content exhibited an activity of 155 μmol $g^{-1}h^{-1}$ at 100°C and atmospheric pressure. Various other catalysts such as Ru, Ni, Co, Pd, and Pt supported on CeO_2 were evaluated with the same weight percentage, all displaying activity at this reduced temperature, with the Fe catalyst showing the highest activity. Notably, Ru catalysts often outperform Fe catalysts when a high weight percentage of Fe is employed, but the Fe catalyst displayed superior activity when used with a lower weight percentage on the catalyst support [12].

KM1 is an iron-based catalyst for ammonia synthesis, meticulously formulated with a selection of promoters. It is widely used in ammonia converters around the world to transform synthesis gas, consisting of hydrogen and nitrogen, into ammonia. Haldor Topsøe has supplied over 1,200 charges of KM1 catalyst, reflecting its widespread adoption and reliability. The high and stable activity of KM1 has led to an impressive track record of long operational lifetimes and record-high production rates in industrial settings [13].

2.1.2. Ruthenium-Based Catalysts

Ruthenium has demonstrated notable efficiency in the production of ammonia, especially when enhanced with alkali metals, outperforming iron catalysts in some cases at atmospheric pressure. These ruthenium catalysts are considered as advanced alternatives to iron catalysts for ammonia synthesis. The industrial viability of ruthenium catalysts is further evidenced by their current use in a commercial ammonia production facility, highlighting their potential for broader industrial application [14].

The Kellogg advanced ammonia process, developed in 1980, utilizes a catalyst composed of ruthenium supported on graphite carbon. Since 1979, when ruthenium was first used as a catalyst for ammonia synthesis supported on graphite carbon, it has garnered significant research interest in the context of ammonia synthesis catalysts.

Various alternative support materials have been explored over the years. Beyond the support materials, researchers have also investigated the effects of ruthenium loading percentage, precursor form, and impregnation method on the catalytic activity. A significant development in this field of catalysts is the identification of the B5-type site as the active site for ruthenium-based catalysts. This site consists of a configuration with three ruthenium atoms in one layer above another layer with two ruthenium atoms. Using a geometric model, it's possible to determine the optimal ruthenium particle size that maximizes the number of B5-type sites, with a ruthenium particle size of 2 nm being identified as the most favorable [8].

Bielawa, Hinrichsen, Birkner and Muhler conducted comprehensive reduction studies and found that the growth of ruthenium particles increases with the reduction temperature, making the reduction temperature critical for achieving the ideal particle size necessary to maximize the number of B5 sites. Additionally, the barium promoter in ruthenium catalysts can increase the number of B5-type sites in the ruthenium catalyst by reshaping the surface of the ruthenium catalyst, as well as by lowering the reduction temperature. An examination of the reaction orders of a barium-promoted and an unpromoted ruthenium catalyst showed that they both utilize the same type of active site and are within experimental limits. Consequently, the enhanced activity in the barium-promoted ruthenium catalyst can be attributed to the increased number of B5-type active sites [15].

Niwa and Aika discovered that lanthanide oxides serve as efficient enhancers for ruthenium catalysts. A key function of these lanthanide additives is to mitigate the effects of hydrogen poisoning, which otherwise hinders the activation of dinitrogen. Their research identified lanthanide oxides, specifically CeO_2, Sm_2O_3, and La_2O_3, as the most effective supports for ammonia synthesis. Notably, high-temperature reduction significantly boosted the catalytic activity. Among these, Ru/Sm_2O_3 and Ru/La_2O_3 exhibited higher activity, while Ru/CeO_2 was distinguished by its stable activity over an extended period. Future investigations will delve into the impact of hydrogen poisoning on these systems [14].

In 2015, Narasimharao, Seetharamulu, Rama Rao and Basahel reported the use of carbon-covered Mg-Al hydrotalcite (CCHT) as a support for ruthenium. Their findings indicated that an ammonia conversion of 0.9% could be achieved at ambient pressure and 600 K when the catalyst was promoted with cesium and barium, with a weight ratio of ruthenium to promoter to support of 10/25.5/25.5/100 [16].

To investigate the influence of ceria morphology, Lin, Liu, Heng, Wang, Ni, Lin and Jiang synthesized both ceria rods and ceria cubes as supports. They found that under identical conditions (1 MPa, 400°C), the ceria rods exhibited an activity more than twice that of the ceria cubes (18 mmol g^{-1} h^{-1} vs. 7.9 mmol g^{-1} h^{-1} at 400°C and 1 MPa). The researchers discovered that the ceria rods had a higher concentration of oxygen vacancies, lower crystallinity, and better dispersion of the ruthenium catalyst compared to the ceria cubes [8].

Wang, Peng, Zhang, Ni, Au and Jiang further explored the use of ceria supports by synthesizing Ru@CeO_2 core-shell particles for ammonia production, featuring ruthenium cores encapsulated in cerium dioxide shells. This approach led to a significant increase in activity, from 4 to 8.5 mmol g^{-1} h^{-1} for the core-shell catalyst compared to a traditionally supported Ru/CeO_2 catalyst under the same conditions (1 MPa, 425°C). The enhanced activity was attributed to the dramatically improved interactions between the ruthenium and the support, which were facilitated by the core-shell catalyst structure. They utilized the perovskite support $LaCoO_3$ and incorporated ruthenium as a B-site dopant instead of adding it to the support surface to create $LaCo_{0.98}Ru_{0.02}O_3$. The activity of the doped perovskite increased from 4.9 to 10.5 mmol g-1 h^{-1} under the same conditions (1 MPa, 450°C) when compared to a traditionally supported Ru catalyst on $LaCoO_3$. This approach revealed a highly synergistic effect between these two species, both of which are active for ammonia synthesis. The substitution of Co with Ru was found to facilitate the dissociative adsorption of N_2 by enhancing the number of Ru clusters and the presence of Co surfaces [8].

Metal hydrides have been explored as catalysts for ammonia production. Kobayashi, Tang, Kageyama, Yamashita, Masuda, Hosokawa & Kageyama proposed a ruthenium catalyst on TiH_2 for ammonia synthesis, observing a modest level of activity and making the intriguing discovery that the H_2 reactant could exchange with lattice hydrogen [17].

Hattori, Tang, Kageyama, Yamashita, Masuda, Hosokawa & Kageyama used CaH_2 as a support material, both with and without the addition of BaO. Their results showed that both catalysts were significantly active at 340°C and atmospheric pressure. There was a noticeable increase in activity compared to the Ru/TiH_2 catalyst, with activities of 2.8 mmol g^{-1} h^{-1} for the Ru/TiH_2 catalyst at 400°C and 5 MPa, and 7.4 mmol g^{-1} h^{-1} for the Ru/CaH_2 catalyst at 340°C and 0.1 MPa, despite the much milder conditions. This significant increase in activity due to changing the metal hydride support highlights this as an interesting area of catalyst development with potential for future improvements [18].

Hattori, Mori, Arai, Inoue, Sasase, Tada, Kitano, Yokoyama, Hara & Hosono recently achieved N_2 activation using a Ru-based catalyst. A solid solution of CaF_2 and CaH_2, converted into a CaFH support at low temperatures, was used as the Ru catalyst support, demonstrating an activity of 50 mol g^{-1} h^{-1} at ambient pressure and near-ambient temperature of 50°C. The strong ionic interactions between Ca^{2+} and H^- in the solid solution were credited by them for its excellent catalytic performance, with the H sites promoting the release of hydrogen atoms [19].

Despite the exceptionally high activity of ruthenium-based catalysts for ammonia synthesis at lower temperatures and pressures, the global production of ruthenium was only 35.5 tonnes in 2017. If a catalyst containing just 2 weight percent of Ru is required for a 300-tonne ammonia synthesis plant, then 6 tonnes of Ru would be needed, representing approximately 17% of the annual global Ru production. Consequently, the cost of Ru would increase significantly. As a result, only about ten ammonia synthesis plants worldwide use Ru-based catalysts, while the rest of the industry is dominated by low-cost fused iron-based catalysts [8].

2.1.3. Electride-Based Catalysts

Even though they are part of the previously known group of ruthenium-based catalysts, this focuses on ruthenium catalysts with electride supports because these materials greatly enhance performance. Electride materials are increasingly being utilized as catalyst supports in electride-based catalysts, a field that has garnered recent attention. These materials are ionic compounds where the anionic role is played by electrons, rather than the typical O^{2-}. However, many of these electride compounds suffer from poor thermal stability. This issue prompted the development of the inorganic electride $[Ca_{24}Al_{28}O_{64}]^{4+}(e^-)_4$ in 2003, which exhibits exceptional stability at temperatures above ambient conditions. Inoue, Kitano, Kim, Yokoyama, Hara & Hosono investigated this electride as a potential support material, given its strong electron-donating and hydrogen-storage capabilities. They employed both solid-phase reaction and hydrothermal methods to synthesize the support material. To assess the impact on surface area and catalytic performance, they varied the temperature at which water and hydroxyl groups were removed during the hydrothermal process, ranging from 873 to 1273 K. When compared to other catalysts like K-Ru/Al_2O_3 and Ru/ZrO_2 at the same temperature and pressure (3 MPa), the $[Ca_{24}Al_{28}O_{64}]4+(e^-)_4$ electride synthesized hydrothermally at 1173K achieved the highest rate of ammonia synthesis among the electride-supported catalysts. Furthermore, it outperformed the Ru-Cs/MgO catalyst under identical pressure and temperature conditions, as reported by them in 2014 [20].

Lu, Li, Tada, Toda, Ueda, Yokoyama, Kitano & Hosono, have been investigating the water-stable electride Y_5Si_3 as a support for ruthenium in ammonia production. In their research, they tested the activity of Y_5Si_3 samples after exposure to distilled water for one hour. They observed that the activity remained unchanged between the wet and dry catalysts. This water stability, while maintaining equivalent activity to traditional ruthenium supports like magnesium oxide (MgO), presents a significant advantage [21].

Table 2.1 provides an overview of the functions and conditions of various electride-based catalysts. Despite the reaction pressure being set at 0.1 MPa for all reported catalysts, this family of catalysts has shown good activity across different electride materials at low temperatures (400°C) [8].

Table 2.1. Chemical composition and activity of selected ruthenium catalysts with electride supports.

Catalyst	Ru content [wt%]	Promoters [wt%]	Reactor temperature [°C]	Reactor pressure [MPa]	WHSV [mL g^{-1} h^{-1}]	NH_3 percentage in reactor outlet [v/v%]	NH_3 synthesis rate [μmol g^{-1} h^{-1}]	Ref.
Ru/HT–C12A7:e^{-}[i]	2	–	340	0.1	18 000	–	2290	[96]
Ru/Ca_2N:e^{-}	1.8	–	340	0.1	36 000	–	3386	[115]
Ru/$Ca(NH_2)_2$	1.8	–	340	0.1	36 000	–	3386	[195]
Ru/Y_5Si_3 NP	10	–	340	0.1	36 000	–	4448	[118]
Ru/C12A7 (microcube)	5	–	400	0.1	36 000	–	5380	[196]
Ru/Y_5Si_3	7.8	–	400	0.1	18 000	–	1875	[117]
Ru/LaScSi	8.3	–	400	0.1	36 000	0.36	5300	[119]
LaRuSi	–	–	400	0.1	36 000	0.492	5340	[120]
CeRuSi	–	–	400	0.1	36 000	–	5480	[120]
CaRuSi	–	–	400	0.1	36 000	–	60	[121]

2.1.4. Cobalt-Based Catalysts

Due to their high activity, cobalt-based ammonia synthesis catalysts have recently garnered the attention of scientists. Cobalt-based catalysts are often used with support materials, similar to ruthenium, but unlike ruthenium, this is primarily for promotional benefits and is not constrained by cost. This allows for a much broader range of weight percentages to be added to these supports and promoters, from just a few weight percentages, as in multi-promoted fused-iron catalysts, to weight percentages comparable to those for ruthenium [8].

Raróg-Pilecka, Karolewska, Truszkiewicz, Iwanek and Mierzwa explored the preparation process for a doubly promoted cobalt catalyst in 2011 using coprecipitated barium- and cerium-enhanced cobalt catalysts. They formed the cobalt and cerium carbonates by adding potassium carbonate to an aqueous solution of either cobalt nitrate or a mixture of cobalt nitrate and cerium nitrate. These carbonates were dried and then subjected to an overnight air treatment at 500°C to produce the oxide catalyst. Barium nitrate was again used as a promoter via the traditional impregnation technique. They measured the activity using a pressure of 6.2 MPa and a gas mole ratio of 3. Once more,

the doubly promoted catalyst exhibited the maximum activity, with a turnover frequency of 0.370 s^{-1} at a temperature of 430°C [8].

By Karolewska, Truszkiewicz, Mierzwa, Kepinski and Raróg-Pilecka in 2012, the impact of cerium addition was investigated. Using cobalt nitrate, cerium nitrate, and potassium carbonate as the precipitant, they created the catalyst by coprecipitation. This led to the production of cerium and cobalt carbonates, which were then transformed into oxide catalysts by air treatment at 500°C. Once more, barium nitrate was used as a promoter utilizing the traditional impregnation technique. The catalyst activity was tested at 400°C, 6.3 MPa of pressure, and a 3 gas mole ratio of H_2/N_2. It was discovered that under these circumstances, a cerium loading of 11.5 wt% generated ammonia at the maximum rate with a value of 3.33 g_{NH3} g^{-1} h^{-1} [8].

Further research on the impact of cerium addition and the preparation process on cobalt catalysts supported on carbon was conducted in 2013 by Karolewska, Truszkiewicz, Mierzwa, Kepinski and Raróg-Pilecka. Their carbon support was made from commercially available, treated activated carbon, and the cobalt and cerium were supported on it using two separate processes. At a pressure of 9.0 MPa and a temperature of 400°C, measurements of the catalytic activity were carried out utilizing a stoichiometric gas flow of nitrogen and hydrogen. Under these circumstances, it was discovered that the impregnation technique of catalyst preparation yields a higher rate, with a rate of 8.16 g_{NH3} g^{-1} h^{-1} for the impregnated catalyst and 4.95 g_{NH3} g^{-1} h^{-1} for the stepwise-impregnated catalyst [8].

When employed to promote a carbon-supported cobalt catalyst, a barium promoter has been shown to increase the stability and activity for the synthesis of ammonia, according to Tarka, Zybert, Truszkiewicz, Mierzwa, Kepinski, Moszynski and Raróg-Pilecka's 2015 report. The catalysts were put to the test at 9 MPa, 400°C, and an H_2/N_2 ratio of 3; it was discovered that under these circumstances, a barium promoter level of 0.68 mmol g^{-1} (C+Co) functioned best, resulting in an ammonia synthesis rate of 1.5 g_{NH3} g_{C+Co}^{-1} h^{-1}.

Co-supported on CeO_2 or carbon and promoted with Ba demonstrates very high activity in these catalysts. Cobalt can be a viable alternative to Ru in terms of price because its cost is much lower than that of Ru. But a thorough investigation of the stability is necessary [8].

2.1.5. Nickel-Based Catalysts

Nickel (Ni) was initially overlooked despite its known activity toward ammonia production and higher cost than iron (Fe) due to its significantly lower activity. However, recent studies have highlighted improved ammonia synthesis activity using Ni-based catalysts. These catalysts work in conjunction with the Ni catalyst as co-catalysts to achieve outstanding results using specially designed support materials [8].

Ye, Park, Lu, Li, Sasase, Kitano, Tada and Hosono successfully achieved excellent activity for a Ni catalyst based on LaN at low temperatures and atmospheric pressure. The nitrogen vacancies on the LaN surface, which weaken the nitrogen triple bond, helped the Ni catalyst overcome its low binding energy and exhibit significant activity. Activities of 2665 and 5500 mol g^{-1} h^{-1} were attained at 340 and 400°C, respectively. This demonstrates that good activity at low temperatures is possible, challenging the conventional belief that Ni-based ammonia catalysts have limited activity. However, to achieve this activity using carefully selected materials to overcome the low binding energy of Ni, the synergistic effect with the support material must be fully realized. This new class of Ni catalyst will function as a type of co-catalyst by using the support material to weaken the nitrogen triple bond [8].

One of the major challenges modern catalysts still face is low-temperature ammonia synthesis, as expensive ruthenium (Ru) catalysts are unable to operate at the low temperatures of fused Fe catalysts. Ni catalysts, however, can withstand these low temperatures, showing excellent activity at temperatures as low as 300°C. Due to their significantly lower cost, fused-Fe catalysts are still preferred in industrial settings over Ru catalysts. Although still more expensive than Fe, these Ni catalysts are substantially

less expensive than Ru and could thus serve as cost-effective catalysts for low-temperature and high-pressure ammonia synthesis facilities [8].

2.1.6. Metal Nitride Catalysts

In addition to metal-based catalysts (Fe, Ru, Co), various metal nitride forms have also been found to exhibit considerable activity in the catalytic production of ammonia.

The concept of ternary nitride systems was a significant advancement in metal nitride catalysts. If two metals are combined to form a ternary nitride, one of which has an excessively high nitrogen adsorption energy and the other of which has an excessively low nitrogen adsorption energy, an ammonia synthesis catalyst can be produced that has a turnover frequency (TOF) closer to the maximum than any nitride created from a single metal [8].

Jacobsen investigated the ternary nitride catalysts Fe_3Mo_3N, Co_3Mo_3N, and Ni_2Mo_3N with promoters. They synthesized these nitrides by combining a metal nitrate salt solution required for the system with an ammonium heptamolybdate solution, drying it, and then calcining it at 400°C for two hours. The resulting $MMoO_4 \cdot xH_2O$ (where M = Fe, Co, and Ni) was heated to 600°C in 4.5% ammonia and a 3:1 H_2-N_2 mixture to generate molybdenum oxide [22].

In 2014, Bion, Can, Cook, Hargreaves, Hector, Levason, McFarlane, Richard & Sardar examined how the preparation process affected the activity of the Ni_2Mo_3N catalyst. They investigated two preparation pathways: the nitridation of $NiMoO_4$ and the nitridation of a mixed-phase precursor created using the Pechini method. Their findings showed that the catalyst made by nitriding $NiMoO_4$ produced an ammonia synthesis rate of less than 15 mol h^{-1} g^{-1}, but the catalyst made by the Pechini method produced an ammonia synthesis rate of 395 mol h^{-1} g^{-1} under the same conditions of ambient pressure and 400°C [23].

Kojima and Aika studied the fabrication process of the Co_3Mo_3N catalyst and its impact on the activity for ammonia synthesis in 2001. They used cobalt molybdate hydrate as a precursor in their preparation. Activity of the catalyst was assessed at 673 K and 0.1 MPa using gas flow rates of 45 mL min^{-1} H_2 and 15 mL min^{-1} N_2. They reported a rate of 652 μmol h^{-1} g^{-1} for the unpromoted Co_3Mo_3N catalyst. When the catalyst was promoted with potassium at a K/Co mole ratio of 0.05, it was demonstrated that this rate increased to 869 μmol h^{-1} g^{-1}. The cesium-promoted catalyst had the highest rate, with a rate of 986 μmol h^{-1} g^{-1} when promoted with cesium at a Cs/Co mole ratio of 0.02 [24].

Cao et al. have documented the synthesis of ternary amides alongside ternary nitrides of transition and alkali metals. They produced $Rb_2[Mn(NH_2)_4]$ and $K_2[Mn(NH_2)_4]$ through a process involving ball-milling the respective metals at ambient temperature under 0.7 MPa of NH_3 pressure. These compounds exhibited activities of 11 mmol g^{-1} h^{-1} for $K_2[Mn(NH_2)_4]$, 6 mmol g^{-1} h^{-1} for $Rb_2[Mn(NH_2)_4]$, and 5.3 mmol g^{-1} h^{-1} for Co_3Mo_3N, all tested at 400°C and 1 MPa. Their performance surpassed that of the most effective ternary nitride catalyst, Co_3Mo_3N, as reported by Cao et al. [25].

In a separate study, Ye, Park, Lu, Li, Sasase, Kitano, Tada and Hosono investigated nitrogen vacancies in nitride catalysts using a Ni-LaN catalyst. They observed an activity of 5500 mmol g^{-1} h^{-1} at 400°C and atmospheric pressure. They attributed this to the weakening of the N triple bond due to H_2 dissociation on the Ni surface and the presence of surface nitrogen vacancies in LaN. Despite Ni's less common use compared to traditional ammonia synthesis catalysts like Ru and Fe, due to its lower N_2 binding energy, they showed that the performance limitations of Ni could be mitigated when paired with LaN, potentially achieving activities similar to those of more costly Ru catalysts [26].

The high cost of nitride catalysts remains a significant barrier to their widespread adoption, especially when compared to fused-Fe catalysts. Further research is essential to evaluate the activity of nitrides under high pressure and their resistance to oxygenates like O_2, H_2O, and CO at elevated temperatures. The tendency of nitrides to convert into oxides or oxynitrides at high temperatures in the presence of oxygenates is a critical aspect that

needs to be understood to assess the viability of nitride-based catalysts for ammonia synthesis. An oxide-based promoter/cocatalyst with functionalized oxygen vacancies, such as $Ce_{0.8}Sm_{0.2}O_2$, has been suggested by Humphreys, Lan and Tao in 2020 as a more stable alternative in oxygenate-rich environments [8].

2.2. Kitenics of the Ammonia Synthesis Reaction

To form new molecules or bonds, the existing chemical bonds between substances often need to be broken. Due to the low activation energy required for this bond breaking, chemical processes can generate complex compounds, ions, and novel radicals without the necessity for catalytic reactions. However, the synthesis of ammonia, similar to many chemical reaction systems, demands a higher activation energy. The presence of catalyst materials accelerates the reaction process by reducing the activation energy compared to what would be required in their absence. Given that each step in a chemical pathway involves activation energy, catalysts are indispensable in the synthesis of ammonia. To understand the relationship between the heat of adsorption and activation energy, it is necessary to develop the process of chemisorption on catalysts. If the nitrogen adsorption step is too slow, it will result in a decreased rate of ammonia production. The type of catalyst employed and the interactions between hydrogen and nitrogen molecules on the catalyst surface are the two primary factors influencing the ammonia synthesis process. The fundamental stages of the reaction pathway outlined in Equation 2.1-2.7 were utilized to execute the mechanism of ammonia production

$$N_2 + * \leftrightarrow N *_2 \tag{2.1}$$

$$N_2 * + \leftrightarrow 2N * \tag{2.2}$$

$$H * + N * \leftrightarrow NH * + * \tag{2.3}$$

$$NH * + * \leftrightarrow NH *_2 + * \tag{2.4}$$

$$NH *_2 + H * NH * + * \leftrightarrow NH *_3 + * \tag{2.5}$$

$$NH *_3 \leftrightarrow NH_3 + * \tag{2.6}$$

$$H_2 + 2* \leftrightarrow 2H* \tag{2.7}$$

where N∗ and H∗ are intermediate activated species.

The role of nitrogen adsorption and desorption is critical in the rate-determining step of the elementary processes involved in ammonia synthesis, particularly when using iron-based catalysts. The reaction mechanism on the surface of the catalyst material can be elucidated through theoretical hypotheses and experimental observations. The rate-determining step offers an estimate of the overall reaction rate for ammonia synthesis. For potential iron catalysts, the rate-determining step could involve the dissociation of nitrogen, the surface reaction of adsorbed species, and the desorption of ammonia. Numerous studies have indicated that the rate-determining step in ammonia synthesis is the dissociation of adsorbed nitrogen.

The Temkin & Pyzhev rate equation is a widely recognized expression for the ammonia production reaction rate. In this model, the rate-determining steps are nitrogen adsorption, hydrogen adsorption, and nitrogen hydrogenation, respectively (Equations 2.1, 2.2, 2.3 & 2.4). The adsorption rate of N_2 can be represented by the Temkin and Pyzhev model, which provides insights into the kinetics of the ammonia synthesis process

$$r_s = kP_{N_2}\exp(-g\theta_N) \tag{2.8}$$

where P_{N_2} is the partial pressure of nitrogen, θ_N is the coverage by N_2 adsorption and k and g are the constants.

In this expression, θ_N is calculated as

$$\theta_N = \frac{1}{f}\ln(AK\frac{(P_{NH_3})^2}{(P_{H_2})^3}) \tag{2.9}$$

where A and K are the equilibrium constants of NH_3 decomposition.

The overall reaction rate equation of the NH_3 production

$$r = k_A P_{N_2} \left(\frac{(P_{H_2})^3}{(P_{NH_3})^2}\right)^{\alpha} - k_B \left(\frac{(P_{NH_3})^2}{(P_{H_2})^3}\right)^{1-\alpha} \quad (2.10)$$

where k_A and k_B are the forward and backward rate constants and α is the reaction constant.

As a function of nitrogen adsorption, the Langmuir-Hinshelwood equation has been presented as the reaction rate equation of ammonia production

$$r = k\, P_{N_2}(1 - \theta_N)^2 = k_s \frac{P_{N_2}}{(1 + K P_{NH_3}/{P_{H_2}}^{1.5})^2} \quad (2.11)$$

where P_{NH_3} is the partial pressure of NH_3, P_{H_2} is the partial pressure of H_2, k_s is constant and P_{N_2}, θ_N and k are as defined before.

The Langmuir-Hinshelwood equation is a model that can be applied to lower-pressure ammonia synthesis processes. This equation is used to evaluate the activity of a catalyst under atmospheric pressure conditions. The Langmuir-Hinshelwood reaction rate equation provides a framework for understanding how the rates of chemical reactions are influenced by the adsorption of reactants onto the surface of a catalyst.

Extensions to the Temkin & Pyzhev equation have been proposed based on various analyses of the ammonia production reaction rate equations. These extensions aim to refine the understanding of the kinetics involved in ammonia synthesis.

Ozaki, Taylor and Boudart suggested that the coverage of nitrogen atoms on the catalyst surface may not be as extensive as previously thought. They proposed a modified reaction rate equation for ammonia synthesis, which takes into account the reduced coverage of nitrogen atoms. Their proposal, offers an alternative perspective on the rate-determining steps and the overall kinetics of the ammonia synthesis process

$$r = k_A\, P_{N_2} - k_B \frac{\frac{(P_{NH_3})^2}{(P_{H_2})^3}}{\left(1 + K_c (P_{NH_3})/(P_{H_2})^{\frac{3}{2}}\right)^{2\alpha}} . \quad (2.12)$$

where K_c is equilibrium constant, P_{NH_3}, P_{H_2}, P_{N_2} and k_A are as defined before. If $K_c(P_{NH_3})/(P_{H_2})^{\frac{3}{2}}) \gg 1$, equation (2.12) can be simplified to the Temkin & Pyzhev rate equation.

To address the shortcomings of equation (2.12), Nielsen proposed an alternative reaction rate equation for the synthesis of ammonia (NH_3)

$$r = k_A P_{N_2} - k_B \frac{(a_{NH_3})^2/(a_{H_2})^3}{(1 + K_c(a_{NH_3})/(a_{H_2})^{\gamma})^{2\alpha}} \quad (2.13)$$

where a_x represents the species activity. The experimental study revealed that 1.5 is the ideal number for γ and P_{N_2}, k_A and k_B are as defined before.

The ammonia synthesis reaction rate over a ruthenium (Ru) catalyst has been calculated similarly to that of an iron (Fe) catalyst by considering the rate-determining step involving nitrogen. A power function reaction rate equation has been employed to approximate the reaction rates in this context.

Table 2.2. Ammonia synthesis reaction rate kinetic parameters over different catalyst types.

Catalyst type	Temperature [K]	Pressure [kPa]	n	m	a
Ru powder	598 553–581	80 101	0.96	−0.72	−0.15 0a
Ru/SiO_2	825–1009 574–671	101 101	1 1	−1 1.25	−1 −0.56
Ru/Celite	619–683	80	1	0	0
Ru/Al_2O_3	610–691 638 500–725	101 80 150	– 1.1 1	– 0.3 0.6	−1.0 −0.74 –
Ru/MgO	593 500–725	80 150	1 0.9	0.66 0.2	−0.78 –
$Ru–Cs^+/Al_2O_3$	595	80	1	−0.55	0
$Ru–K^+/Al_2O_3$	500–725	150	1	−0.3	–
$Ru–Cs^+/MgO$	548	80	1	−0.43	−0.12
$Ru–K^+/MgO$	500–725	150	1	−0.5	–
Ru powder–Cs^+	598	80	0.95	−0.9	−0.07
$Ru–K/Al_2O_3$	500–725	150	0.9	−1.1	–
Ru–K/MgO	500–725	150	1.2	−0.5	–

Various researchers have investigated the sequence of adsorption and desorption processes during the production of elementary species in ammonia synthesis. From experimental data, kinetic parameters have been derived. Table 2.3 compiles the rate equations and microkinetic response mechanisms. Three models have been analyzed to determine the reaction rate of the ammonia production process. Identifying the mechanism of the surface reaction is crucial for calculating the rate of ammonia production. Stoltze and Norskove suggested the reaction rate mechanism for Model I, and Bowker proposed Models II and III.

Table 2.3. Ammonia synthesis reaction rate equations and reaction kinetics.

Rates of forward reactions	Model I	Rates of reverse reactions
$2\times10^{1}P_{N_2}\theta^{*}$	$N_2+*\rightleftharpoons N_2^{*}$ (1)	$2\times10^{14}e^{-43/RT}\theta_{N2}^{*}$
$4\times10^{9}e^{-29/RT}\theta_{N2}^{*}\theta^{*}$	$N_2^{*}+*\rightleftharpoons 2N^{*}$ (2)	$1\times10^{9}e^{-155/RT}(\theta_{N2}^{*})^{2}$
$2\times10^{9}e^{-81/RT}\theta_{H}^{*}\theta_{N}^{*}$	$N^{*}+H^{*}\rightleftharpoons NH^{*}+*$ (3)	$1\times10^{7}e^{-23/RT}\theta_{NH}^{*}\theta^{*}$
$1\times10^{13}e^{-36/RT}\theta_{NH}^{*}\theta_{H}^{*}$	$NH^{*}+H^{*}\rightleftharpoons NH_2^{*}+*$ (4)	$1\times10^{12}\theta_{NH_2}^{*}\theta^{*}$
$4\times10^{13}e^{-39/RT}\theta_{NH2}^{*}\theta_{H}^{*}$	$NH_2^{*}+H^{*}\rightleftharpoons NH_3^{*}+*$ (5)	$2\times10^{13}\theta_{NH_3}^{*}\theta^{*}$
$4\times10^{12}e^{-39/RT}\theta_{NH3}^{*}$	$NH_3^{*}\rightleftharpoons NH_3+*$ (6)	$2\times10^{3}P_{NH_3}\theta^{*}$
$7\times10^{1}P_{H_2}(\theta^{*})^{2}$	$H_2+2^{*}\rightleftharpoons 2H^{*}$ (7)	$3\times10^{13}e^{-94/RT}(\theta_{H}^{*})^{2}$
Rates of forward reactions	**Model II**	**Rates of reverse reactions**
$3\times10^{1}P_{N_2}\theta^{*}$	$N_2+*\rightleftharpoons N_2^{*}$ (1)	$2\times10^{10}e^{-46/RT}\theta_{N2}^{*}$
$3\times10^{6}e^{-31/RT}\theta_{N2}^{*}\theta^{*}$	$N_2^{*}+*\rightleftharpoons 2N^{*}$ (2)	$3\times10^{12}e^{-199/RT}(\theta_{N}^{*})^{2}$
$1\times10^{12}e^{-65/RT}\theta_{H}^{*}\theta_{N}^{*}$	$N^{*}+H^{*}\rightleftharpoons NH^{*}+*$ (3)	$2\times10^{12}e^{-19/RT}\theta_{NH}^{*}\theta^{*}$
$8\times10^{11}e^{-65/RT}\theta_{NH}^{*}\theta_{H}^{*}$	$NH^{*}+H^{*}\rightleftharpoons NH_2^{*}+*$ (4)	$2\times10^{12}e^{-19/RT}\theta_{NH2}^{*}\theta^{*}$
$7\times10^{12}e^{-65/RT}\theta_{NH2}^{*}\theta_{H}^{*}$	$NH_2^{*}+H^{*}\rightleftharpoons NH_3^{*}+*$ (5)	$2\times10^{12}e^{-19/RT}\theta_{NH3}^{*}\theta^{*}$
$1\times10^{13}e^{-53/RT}\theta_{NH3}^{*}$	$NH_3^{*}\rightleftharpoons NH_3+*$ (6)	$2\times10^{2}P_{NH_3}\theta^{*}$
$3\times10^{3}P_{H_2}\theta^{*}$	$H_2+*\rightleftharpoons H_2^{*}$ (8)	$2\times10^{13}\theta_{H2}^{*}$
$3\times10^{12}\theta_{H2}^{*}\theta^{*}$	$H_2^{*}+*\rightleftharpoons 2H^{*}$ (9)	$3\times10^{13}e^{-92/RT}(\theta_{H}^{*})^{2}$
Rates of forward reactions	**Model III**	**Rates of reverse reactions**
$3\times10^{1}P_{N_2}\theta^{*}$	$N_2+*\rightleftharpoons N_2^{*}$ (1)	$2\times10^{10}e^{-46/RT}\theta_{N2}^{*}$
$2\times10^{9}e^{-31/RT}\theta_{N2}^{*}\theta^{*}$	$N_2^{*}+*\rightleftharpoons 2N^{*}$ (2)	$2\times10^{9}e^{-144/RT}(\theta_{N}^{*})^{2}$
$1\times10^{11}e^{-54/RT}\theta_{H}^{*}\theta_{N}^{*}$	$N^{*}+H^{*}\rightleftharpoons NH^{*}+*$ (3)	$2\times10^{12}e^{-17/RT}\theta_{NH}^{*}\theta^{*}$
$8\times10^{10}e^{-54/RT}\theta_{NH}^{*}\theta_{H}^{*}$	$NH^{*}+H^{*}\rightleftharpoons NH_2^{*}+*$ (4)	$2\times10^{12}e^{-17/RT}\theta_{NH2}^{*}\theta^{*}$
$7\times10^{11}e^{-54/RT}\theta_{NH2}^{*}\theta_{H}^{*}$	$NH_2^{*}+H^{*}\rightleftharpoons NH_3^{*}+*$ (5)	$2\times10^{12}e^{-17/RT}\theta_{NH3}^{*}\theta^{*}$
$1\times10^{13}e^{-53/RT}\theta_{NH3}^{*}$	$NH_3^{*}\rightleftharpoons NH_3+*$ (6)	$2\times10^{2}P_{NH_3}\theta^{*}$
$3\times10^{3}P_{H_2}\theta^{*}$	$H_2+*\rightleftharpoons H_2^{*}$ (8)	$2\times10^{13}\theta_{H2}^{*}$
$3\times10^{12}P_{H_2}\theta^{*}$	$H_2^{*}+*\rightleftharpoons 2H^{*}$ (9)	$3\times10^{12}e^{-92/RT}(\theta_{H}^{*})^{2}$

The Temkin & Pyzhev rate equation (2.8) was adjusted by incorporating a second rate-determining step, which involves the addition of hydrogen to the adsorbed nitrogen, as shown below

$$r = k\,P_{N_2}{}^{1-\alpha} \times \frac{(1 - (\frac{\frac{1}{K}(P_{NH_3})^2}{(P_{N_2}(P_{H_2})^3}))\,)}{(\frac{1}{P_{H_2}} + \frac{\frac{1}{K}(P_{NH_3})^2}{(P_{N_2}(P_{H_2})^3})^{\alpha} \times (1 + \frac{1}{P_{H_2}})^{1-\alpha}} \qquad (2.15)$$

where P_{NH_3} , P_{H_2}, P_{N_2}, α and k are as defined before.

Table 2.4 presents the percentage error of the NH_3 reaction rate model equations. These models show that at reduced operating pressures, the Temkin rate law equation leads to greater inaccuracies. The effectiveness of all rate equations in predicting ammonia synthesis across different catalysts can also be evaluated. While the power rate law equation is favored for its simplicity in analyzing new catalytic materials, establishing its parameters necessitates specialized experimental conditions, which can be quite time-consuming. Conversely, alternative rate equations can offer insights into the NH_3 synthesis process and estimate the rate of dissociation adsorption by leveraging the basic steps of the ammonia synthesis reaction mechanism [7].

Table 2.4. Error % results of rate models compared with experimental data.

P (atm)	Inlet flow rate [cm^3 STP/min]	Space velocity [h^{-1}]	Ozaki rate	Temkin rate	Langmuir rate	Power rate
107	221	11,600	0.27	3.90	0.33	0.50
107	305	16,000	0.28	1.36	0.68	0.31
107	449	23,500	0.29	0.02	0.87	0.72
107	458	24,000	0.29	0.04	0.87	0.73
107	899	47,100	0.32	0.84	0.98	0.96
214	267	14,000	0.62	1.66	0.62	0.15
214	305	16,000	0.62	0.95	0.73	0.39
214	458	24,000	0.61	0.28	0.90	0.79
214	519	272,000	0.61	0.48	0.93	0.85
214	954	50,000	0.60	0.90	0.99	0.97
214	1634	85,600	0.60	0.97	1.00	0.99
320	305	16,000	0.81	0.77	0.75	0.43
320	313	16,400	0.81	0.67	0.76	0.46
320	458	24,000	0.81	0.36	0.91	0.80
320	574	30,100	0.81	0.56	0.94	0.87
320	1527	80,000	0.80	0.97	1.00	0.99

2.3. Membrane

Currently, the primary source of hydrogen, which is produced through the steam reforming of hydrocarbons, is co-located with ammonia production in large-scale industrial plants. However, for the production of "green" ammonia using hydrogen generated by renewable electrolysis, modular manufacturing techniques that align with the distributed nature of wind and solar energy sources would be beneficial. This approach requires the development of more economical and favorable conditions for ammonia synthesis.

One strategy has been the development of catalysts that can operate at lower temperatures. While differential reactors have achieved high specific rates, demonstrating improvements under real-world conditions of high pressure and conversion has been challenging. An alternative approach is to use absorption instead of traditional separation processes, which could enable scalable ammonia production at lower operating pressures. Moreover, the integration of catalysts with absorbents might allow the conversion to exceed typical equilibrium limitations.

Membranes, as an alternative separation method, could play a critical role in enabling modular ammonia production at low pressure (30 bar). However, separating ammonia from nitrogen and especially hydrogen is quite challenging [27].

Researchers are exploring the development of membranes that can efficiently separate the mixed gases resulting from the Haber process. The ideal membrane would exhibit high selectivity for ammonia while being impermeable to hydrogen and nitrogen. It should also be capable of operating at the same high temperature and pressure as the reactor and allow argon to pass through.

Membrane separations can be selective based on specific chemistry or molecular size. Since the ammonia molecule is intermediate in size between hydrogen and nitrogen, size-based membranes are not particularly effective in this context. Chemically selective membranes, however, show greater promise [28].

Studies on ammonia separation using membranes can be categorized into two main types: those employing molten salts and those using polymer films. Research with molten salts is conducted at high temperatures similar to those used in ammonia production. Liquid membranes sustain the molten salt within the pores of a stainless steel mesh. These membranes operate via a mobile carrier mechanism. For example, when zinc bromide is in its molten state, ammonia molecules preferentially interact with Zn^{2+} ions to form a complex that diffuses across the membrane and releases ammonia on the other side. This carrier-assisted diffusion occurs alongside normal diffusion, where ammonia, hydrogen, and nitrogen simply dissolve in the membrane and diffuse through it.

In ammonia separation utilizing polymer films, materials such as polyvinylammonium thiocyanate and perfluorinated copolymers have been highlighted. The glassy polyvinyl ammonium thiocyanate becomes rubbery in the presence of ammonia and is approximately 4,000 times more selective for ammonia than for hydrogen or nitrogen. This remarkable selectivity in a rubbery polymer film is noteworthy. The membrane likely does not operate through a mobile carrier mechanism, which has been responsible for several highly selective membrane separations in the past. Instead, the process seems to depend on the solubility of ammonia in ammonium salts. When ammonia interacts with polyvinyl ammonium thiocyanate, it is believed to form a solution of polyvinyl amine and ammonium thiocyanate. The exceptional solubility of ammonia in ammonium thiocyanate is presumably why ammonia dissolves in this polymer solution.

Ammonia-selective membranes can also be fabricated from perfluorinated copolymers. Although hydrogen has a much lower permeability in these membranes compared to pure ammonia, the selectivity observed when separating ammonia-hydrogen mixtures can be significantly lower. The theory suggests that the selectivity of these films arises from a network of molecular channels through which ammonia travels after undergoing reversible interactions with sulfate groups. This system has been proposed as a form of carrier-aided transport, but no experiment has yet been conducted to rigorously confirm such a process.

He and Cussler chose poly (perfluoro-sulfonic acid) membranes, commonly known by the Du Pont brand name "Nafion," for their research. They observed that temperature significantly affects the flow of ammonia through different types of perfluoro-sulfonic acid membranes. The nitrogen flows exhibit consistent behavior. At room temperature and a pressure difference of 270 kPa, the flow is less than 10^{-9} mol cm^{-2} s^{-1}, indicating a permeability of 0.4 barrier, or less than $3x10^{-8}$ cm s^{-2}, which is typical for many polymer films. The flux increases with temperature. The ammonia fluxes, however, increase very sharply. At room temperature, these fluxes have a permeability of $1.0x10^{-4}$ cm^2 s^{-1}, or 1300 barrier, corresponding to fluxes of about 3.0 x 10^{-6} mol cm^{-2}sec at a pressure difference of 270 kPa. This suggests an ammonia selectivity over nitrogen of more than 3000:1. The permeability decreases with increasing temperature, reaching a minimum value at around 150°C. Beyond this point, the flux increases again, reaching 1.2 x 10^{-6} mol cm^{-2} s^{-1} at 240°C. Despite the unique behavior that reduces selectivity, the membrane remains approximately sixty times more permeable to ammonia than to nitrogen or hydrogen at 240°C. Additionally, the ammonia flow strongly depends on the counterion of perfluoro sulfonic acid. The permeability of ammonia in perfluorosulfonic acid films specifically decreases at 21°C in the following order: H^+> Na^+> Ag^+> NH_4^+> Li^+> K^+. Similar permeability ordering has been observed for other gases diffusing through perfluorocarboxylate membranes [29].

In their experiment, Bhown and Cussler prepared two types of membranes: polymer membranes and salt membranes. They showed that the ammonia flow through 35-µm poly (vinyl ammonium thiocyanate) membranes is minimal until the ammonia pressure exceeds 100 kPa, after which it begins to rise fairly linearly. At higher ammonia pressures, the nitrogen and hydrogen fluxes, which are tiny at low ammonia pressures, are still too small for measurements. Based on the sensitivity of their concentration measurements, they calculated that the nitrogen and hydrogen flows are at least 3000 times less than the ammonia flux. Consistent with their previous work, these membranes are at least 3000 times more selective for ammonia than for nitrogen and hydrogen.

To create ammonium thiocyanate membranes, inert microporous polypropylene membranes were dipped in a solution of this salt and then exposed to 100 kPa of ammonia before being air-dried. The resulting membrane has a consistent thickness and becomes transparent at room temperature at ammonia pressures greater than 30 kPa, resembling a supported liquid membrane at these pressures. Ammonia fluxes are minimal below 30 kPa; at higher pressures, they vary linearly with ammonia pressure. The selectivities appear to be comparable to those found in poly (vinyl ammonium thiocyanate). The temperature variation of the flux also seems similar, as does the flow. Notably, the ammonium flow across NH_4SCN membranes appears to extrapolate to zero at zero ammonia pressure [30].

Wei, Lucero, Crawford, Way, Wolden and Carreon fabricated ZIF-21 membranes through a secondary seeded growth method, resulting in a sheet-like morphology. The sheet-like form and crystallinity of ZIF-21 were confirmed by high-resolution transmission electron microscopy. After evacuating gases under vacuum at 200°C for at least 24 hours, room temperature adsorption isotherms (293 K) were obtained for ZIF-21 crystals. Ideal adsorption selectivities for NH_3/N_2 and NH_3/H_2 were calculated at 1 atm (1013 mbar). The selectivity was found to be 49.3 for NH_3/H_2 and 58.3 for NH_3/N_2. The low-pressure uptake characteristic of the NH_3 isotherm suggests that ZIF-21 crystal pores exhibit a significant amount of adsorption. The results confirm that NH_3, being the most polarizable molecule, preferentially adsorbs on the surface of ZIF-21. Specifically, the greater polarizability of NH_3 ($22.2 \times 10^{25} cm^{-3}$) compared to N_2 ($17.7 \times 10^{25} cm^{-3}$) and H_2 ($8.2 \times 10^{25}\ cm^{-3}$) would thermodynamically favor the separation of ammonia over nitrogen and hydrogen. In response to the preferred interaction of ammonia with the polar walls of ZIF-21 (due to the presence of uncoordinated nitrogen atoms of purine), they developed and evaluated ZIF-21 membranes for the separation of ammonia from nitrogen and hydrogen.

Ammonia permeances reached 1727 GPU, with optimal selectivities of 35 for NH_3/N_2 and 12 for NH_3/H_2, respectively. Specifically, for both gas combinations, the polar-polar interaction between ammonia and the linker's polar channels caused ammonia to preferentially adsorb, which facilitated the thermodynamic separation of ammonia from nitrogen and hydrogen. Differences in diffusivities were another separation mechanism for the NH_3/N_2 gas combination. The faster hydrogen diffusivity made the kinetic contribution for the NH_3/H_2 gas pair a powerful competitive separation mechanism. Separation selectivities as high as 7.6 for NH_3/N_2 were achieved for gas mixtures with a 13.8:86.2 NH_3/N_2 and NH_3/H_2 composition. The separation selectivity was poor for mixtures of NH_3/H_2, which was explained by the very competitive kinetic contribution [27].

Phillip, Martono, Chen, Hillmyer, & Cussler investigated five membranes, all of which had a bicontinuous structure and a phase that was significantly more permeable to ammonia than the others. The gas-filled voids in the alumina membranes are surrounded by solid alumina particles. The idealized structure of Nafion is represented by a perfluorinated hydrophobic phase encircling a sulfonated hydrophilic phase, often described as a pair of inverted micelles in contact. In the three copolymer-templated films, a hydrophobic phase made of polycyclooctene or polydicyclopentadiene surrounds a hydrophilic phase made of polystyrene sulfonate. Each of these membranes can be thought of as having "pores" due to the hydrophilic nature of ammonia. The statistics for Nafion stand in sharp contrast. Due to diffusion in polymer rather than in diluted gas, the nitrogen and hydrogen permeabilities are almost 10,000 times lower than those in the alumina membrane. Surprisingly, the ammonia flux is approximately 400 times larger than the nitrogen and hydrogen fluxes. Nitrogen and hydrogen have fluxes in more familiar units of around 23.5×10^{-17} kmol m (m^{-2} s^{-1} Pa^{-1}) (700 barrers), but ammonia has a flow of more than 10.0×10^{-14} kmol m (m^{-2} s^{-1} Pa^{-1}) (300,000 barrers). This suggests that Nafion has an optimal selectivity for ammonia over hydrogen and nitrogen of more than 400:1 (based on pure gases) [28].

In the study by Laciak, Pez & Burban a membrane made of molten $LiNO_3$ supported on a steel mesh was brought to an initial steady state using a pure N_2 feed gas (30 sccm) [sccm = cm^3 (STP) min^{-1}] and a helium sweep stream (30 sccm) at 76 cmHg. The concentrations of these gases in the permeate stream were then regularly monitored while the N_2 stream was replaced with NH_3/N_2 mixtures of increasing proportions of NH_3. The average NH_3 permeabilities and selectivities for certain NH_3/N_2 feed gas mixtures were determined during three days of steady-state operation. It is evident that this membrane achieves a fair separation of NH_3 from N_2, especially for feed mixtures with modest amounts of NH_3. Compared to standard organic polymer membranes, the NH_3 permeability of 10^3-10^4 barrer is 100–1000 times greater. It becomes slightly more significant at lower feed pressures, suggesting a chemically aided transport mechanism with lithium ammoniate complexes, $Li(NH_3)^{+n}$, as the most plausible carrier species. Unfortunately, at this time, it is not feasible to further evaluate the NH_3 transport mechanism since the only information provided for the absorption of NH_3 by molten $LiNO_3$ is a Henry's law constant at <5 cmHg [31].

Membranes made by suspending molten $ZnCl_2$ in a stainless steel mesh were tested for their ability to separate NH_3 from N_2 at 250°C, 300°C, and 350°C. The system was brought to a steady state at each temperature using pure N_2 as the initial supply gas (30 sccm, 80 cmHg) and He sweep stream (20 sccm, 80 cmHg). Then, at the same flow rate and pressure, various NH_3/N_2 mixtures ranging from 10% to 100% NH_3 were used to replace the N_2 flow. Over 21 days of continuous operation, they observed no decline in membrane function, despite the moderate corrosiveness of molten $ZnCl_2$. The amount of NH_3 present in the helium-swept permeate stream for each feed gas composition, as well as the estimated NH_3 permeability, was recorded. Again, an extremely high NH_3 permeability of 10^5 barrer was achieved. The very low N_2 permeability was always less than 10 barrer. Due to the detection limits of their instrument, they believe that the membrane's selectivity, $\alpha(NH_3/N_2)$, is at least 1000 [31].

3. MATHEMATICAL MODELING

3.1. Description of the Cascade System

Figure 3.1 illustrates the setup of a cascade system comprising packed-bed reactors (PBRs) and microchannel membrane heat exchangers, which is analyzed using 2D, non-isothermal, steady-state simulations in ANSYS and MATLAB. Reaction (1.1) occurs adiabatically with an iron-based catalyst in each PBR, where the maximum temperature is restricted to 623K to maintain membrane stability. The feed is introduced at 573K, 50 bar, with a flow rate of 3.33 mol s^{-1} and a hydrogen-to-nitrogen ratio of 3. This inlet molar flow rate is based on the hydrogen output from a 1 MW electrolyzer, equivalent to 2.5 mol s^{-1} [32]. The adiabatic PBR effluent, consisting of an H_2-N_2-NH_3 mixture catalyzed by iron-based catalyst, travels through the reaction channels, while nitrogen sweep gas in the permeate channels controls the effluent temperature. Each subsequent micro-Heat Exchanger unit reduces the temperature at the end of each reactor bed to about 573K, which is then used as the inlet temperature for all PBRs. Zirconia-supported $ZnCl_2$-immobilized molten salt (IMS) membranes separate the permeate and reaction channels, aiding in NH_3 transport. The model incorporates mass, momentum, and energy conservation in both the PBR and microchannel membrane Heat Exchangers, with NH_3 transport across the membrane described by Fick's law. After membrane separation and cooling in the micro-HEx unit, the exit from the reaction channel proceeds to the next PBR for NH_3 synthesis.

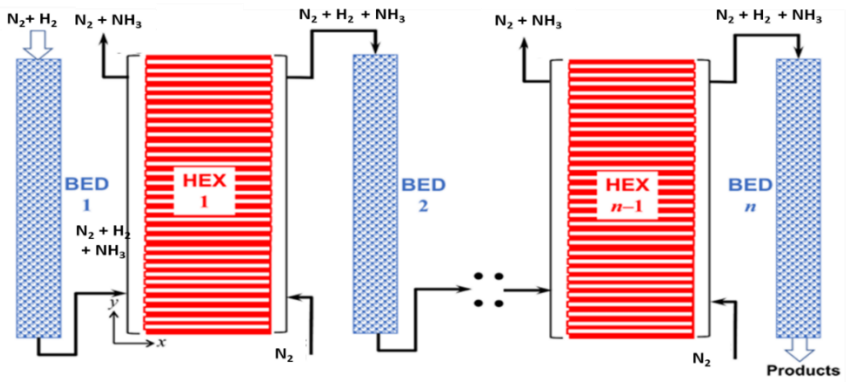

Figure 3.1. Flow diagram of the cascade reactor system.

3.2. Modeling of the PBR Units

The modeling of packed-bed reactors (PBRs) and micro-Heat Exchanger units is performed separately to simulate the cascade system. The tubular PBRs are analyzed under steady-state conditions, ignoring heat transport resistances, external heating, radial gradients, channeling effects, and diffuse transport phenomena. Modeling of the Packed-Bed Reactors involves conservation of mass, energy, and momentum, along with empirical correlations for estimating fluid properties, detailed in Table 3.1 [33].

Table 3.1. Model equations for the packed–bed reactor units in cascade reactor system.

Species Mass Equations	$\frac{dF_{N_2}}{dW} = R_{N_2} = -r; \frac{dF_{H_2}}{dW} = R_{H_2} = -3r; \frac{dF_{NH_3}}{dW} = R_{NH_3} = 2r;$
Energy Equation	$\frac{dT}{dW} = \frac{\sum_{rxn}(-\Delta H_{rxn})(r_{rxn})}{\sum_i F_i c_{p,i}}$
Pressure Drop Equation	$\frac{dP}{dW} = -\frac{\beta_0}{\rho_{cat} A_c (1-\varepsilon_{bed})} \frac{P_o}{P} \frac{T}{T_o} \frac{F_{Total}}{F_{Total,o}}$
	$\beta_0 = \frac{G}{\rho_m g d_p} \left(\frac{1-\varepsilon_{bed}}{{\varepsilon_{bed}}^3}\right) \left[\frac{1150(1-\varepsilon_{bed})\mu_m}{d_p} + 1.75G\right]; \; G = \rho_m . u$

where F_i represents flow rate of the component, W represents catalyst weight, T represents temperature, r is reaction rate, $G, \rho_m, g, d_p, \varepsilon_{bed}$ and μ_m are constants.

The N_2 and H_2 gases are uniformly distributed across the cross-section of the tubular PBRs, moving in a plug-flow manner along the catalyst bed. To assume plug flow pattern, there are constraints such as ensuring that the ratio of the length to the particle diameter is greater than 50, the ratio of the reactor diameter to the particle diameter is greater than 10, and the pressure drop per PBR is less than 3% [33]. Variations in temperature, molar flow rate, and pressure are determined using a one-dimensional (1D) pseudo-homogeneous model, which involves solving a set of nonlinear ordinary differential equations (ODEs) based on these assumptions (Table 3.1) [34]. The aim is to observe the

effect of the inlet temperature on reactor performance, to improve the ammonia production process, and to develop new configurations in order to create a more efficient system.

The inlet conditions for the first PBR are as follows

$$W_{PBR_1} = 0\ kg;\ F^{in}_{PBR_1} = F_0 = 3{,}33\ mol\ s^{-1};\ T^{in}_{PBR_1} = 573K;\ P^{in}_{PBR_1} = 50\ bar \quad (3.1)$$

where F, W, T and P are as defined before.

A trial-and-error method is used to determine the catalyst weight, considering the outlet temperature of 623K (the thermal stability limit of the membrane) and the inlet temperature of 573K. The catalyst weight is determined by numerically integrating a set of ODEs and their initial conditions (Table 3.1) using the "ode15s" solver in MATLAB version 2023b. The output values from each PBR serve as the inlet conditions for the micro-Heat Exchangers. For the membraneless scenario, the initial conditions for modeling the remaining PBRs are provided, with the role of micro-Heat Exchangers being to cool the reactive stream to 573K (±2)

$$W_{PBR_k} = 0, (2 \leq k \leq n);\ F^{in}_{PBR_k} = F^{exit}_{PBR_{k-1}};\ T^{in}_{PBR_k} = 573K;\ P^{in}_{PBR_1} = P^{exit}_{HEX_{k-1}}. \quad (3.2)$$

When using a membrane, the total molar flow rate at PBR_{k-1} changes due to material transport across the membrane. The conditions for this scenario are

$$W_{PBR_k} = 0, (2 \leq k \leq n);\ F^{in}_{PBR_k} = F^{exit}_{HEX_{k-1}};\ T^{in}_{PBR_k} = 573K;\ P^{in}_{PBR_1} = P^{exit}_{HEX_{k-1}}. \quad (3.3)$$

Given that the maximum bed temperature limit is not surpassed, the catalyst weight for PBR1 is calculated to be 1.2×10^{-1} kg, and this same weight is applied to the other reactors within the cascade system. In determining the dimensions of the PBRs constraints of plug flow pattern are taken into account. The reactor length is specified as 2.5×10^{-1} m, and the reactor diameter is 1.5×10^{-1} m. The total number of PBRs is established by restricting the friction pressure loss between the inlet and outlet of the cascade system to 10% (±1), based on comparisons of cumulative nitrogen conversion and productivity. The sizing details for PBR units under a total flow rate of 3.33 mol s^{-1} are tabulated in Table 3.2. Notably, this sizing configuration remains uniform across all PBRs.

Table 3.2. Dimension and constraint calculation of the PBR units.

Reactor Length	Reactor Diameter	L/D_p	D/D_p	%ΔP
0.25 m	0.15 m	84.9	50	1.2

The density and porosity of the iron-based catalyst (commercial KM1 catalyst produced by Haldor Topsøe A/S; composition: 94% Fe, 2.8% CaO, 2.5% Al_2O_3, and 0.6% K_2O [35]) are assumed to be 4.8×10^3 kg m^{-3} and 4.4×10^{-1}, respectively, and the iron-based catalyst particles, which are spherical in shape, have an average diameter of 3×10^{-3} m [36].

To effectively solve Equations in Table 3.1 numerically, it is crucial to understand how temperature influences Reaction (1.1). The iron-based catalyst plays a significant role in enhancing the conversion of N_2, while excluding the consideration of gas-phase reactions and the effects of reactor materials. Equation (3.4) provides a description of the kinetics of Reaction (1.1) as it occurs on the KM1 catalyst under commercial conditions, which are consistent with the operating parameters mentioned. Specific parameters related to Equation (3.4) are provided in detail in Equation (3.5) and Table 3.3 [37].

$$r = k' \frac{(p_{N_2} - p_{NH_3}^2 / p_{H_2}^3 K')}{(1 + p_{NH_3} / p_{H_2}^{1.5} K_1 + p_{H_2}^{0.5} / K_2)^2} \tag{3.4}$$

$$parameter\ (k', K_1, K_2, K') = A e^{\frac{-E_a}{RT}} \tag{3.5}$$

where k', K_1, K_2 and K' are consants and p_{N_2}, p_{NH_3} and p_{H_2} are as defined before.

Table 3.3. Rate law parameters and the reaction equilibrium constant.

Parameter	***A***	***E_a (kJ mol^{-1})***	***Units***
k'	3.74×10^1	6.6	kmol m^{-3} s^{-1} bar^{-1}
K_1	2.7×10^{-2}	27.1	$bar^{-0.5}$
K_2	2.2×10^3	48.0	$bar^{0.5}$
K'	2.0×10^{-12}	–101.6	bar^{-2}

3.3. Modeling of the Microchannel Membrane Heat Exchanger Units

Figure 3.2a shows the micro-Heat Exchanger units. In a membraneless configuration, channels for the cooling and reactive streams, which contain counter-currently partitioned coolant and effluent streams from the previous PBR, are separated by a stainless-steel wall with a thermal conductivity of 16.3 W m^{-1} K^{-1}. Each rectangular channel measures 3×10^{-4} m in height (H) and 6×10^{-4} m in width (W), with a micro-Heat Exchanger unit length (L) of 1.5×10^{-1} m, chosen for ease of machining [38]. The thickness of the stainless-steel wall between channels in the y- and z-directions is 1×10^{-3} m. Heat transfer occurs only between the cooling and reactive stream channels along the y- and x-coordinates. The exothermic heat in the reaction channels is absorbed by the sweep gas, which acts as a coolant and flows through the adjacent permeate channels. Assumptions include even distribution of reactive and coolant streams to each channel and neglecting heat loss to the environment. The pressure difference between the inlet channels is zero. These simplifications reduce the multichannel Heat Exchanger behavior to the unit cell depicted in Figure 3.2b. The coolant is introduced at a constant rate of 4.91×10^{-1} m s^{-1}, 50 bar, and 573K, matching the inlet temperature of the subsequent PBR unit. The flow of N_2+H_2+NH_3 exiting the PBR is divided into each channel of the micro-HEx unit. The total number of channels is determined by the ratio of the flow in each channel to the total flow. Using this information, along with the distances between channels and the channel dimensions, the sizing of the micro-HEx is calculated. These calculations are presented in Table 3.4.

The ratio between the reactive stream and coolant flow rates is adjusted based on the channel length to minimize the temperature difference between the streams. Further extending the channels does not improve heat transfer.

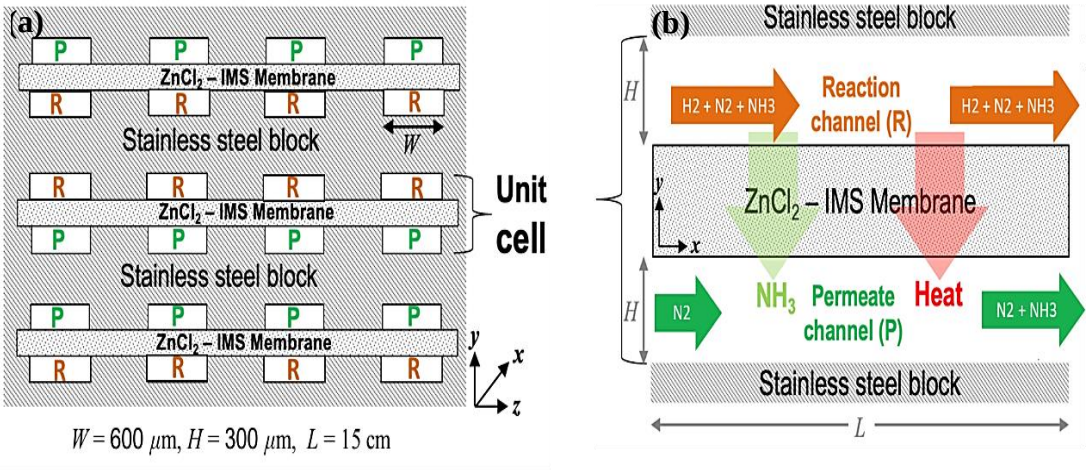

Figure 3.2. Schematic drawings of (a) the membrane integrated microchannel heat exchanger and (b) the unit cell. Drawings are not to scale.

Table 3.4. Dimensions of the micro-HEx units.

Channel Length (mm)	150	H/W Ratio	1.625
Channel Height (mm)	0.3	Number of Reaction Channels	3.72×10^5
Channel Width (mm)	0.6	Total Number of Channels	7.44×10^5
Wall Thickness (mm)	1	Block Height (m)	1.25
Repeating Unit Height (mm)	2.6	Block Width (m)	1.25
Repeting Unit Width (mm)	1.6	Block Volume (m^3)	0.236

Negligible differences between 2D and 3D models with similar conditions and channel geometries allow for the disregard of gradients in the z-direction. The transport phenomena in the cooling and reactive stream channels, as well as heat transfer across the solid wall of the membraneless micro-Heat Exchanger units, are quantified using the model equations provided in Table 3.5.

Table 3.5. Model equations used to simulate the micro-HEx unit (FP: Fluid phases SW: Solid wall).

Continuity Equation	$\nabla.(\rho_m \vec{\boldsymbol{v}}) = 0$
Momentum eq. (FP)	$\nabla.(\rho_m \vec{\boldsymbol{v}}\vec{\boldsymbol{v}}) = \nabla P + \nabla.\left[\mu_m\left(\nabla\vec{\boldsymbol{v}} + (\nabla\vec{\boldsymbol{v}})^T - \frac{2}{3}(\nabla.\vec{\boldsymbol{v}})I\right)\right]$
Species Mass eq. (FP)	$\nabla.(\rho_m \vec{v} Y_i) = -\nabla.\vec{J_i};\ \vec{J_i} = -\rho_m D_{i,m}\nabla Y_i$
Energy eq. (FP)	$\nabla.\left(\rho_m c_{p,m}\vec{v}\,T\right) = \nabla.(k_m \nabla \mathrm{T})$
Energy eq. (SW)*	$\nabla.(k_w \nabla \mathrm{T}) = 0$

*Last is used in modeling the membraneless micro–HEx unit in which reactive stream and cooling channels are separated by a solid wall.

According to Laciak, Pez & Burban [31], the transfer of NH_3 across the $ZnCl_2$ IMS membrane occurs via diffusion-controlled facilitated transport, where the flux is influenced by the permeability, membrane thickness, and the partial pressure difference between the channels, showing a first-order dependence as

$$J_{NH_3} = \frac{Perm_{NH_3}}{t_{mem}}\left(P_R{}^{NH_3} - P_P{}^{NH_3}\right) \tag{3.6}$$

where J is flux, $Perm_{NH_3}$ is permability of ammonia, t_{mem} is thickness of the membrane, $P_R{}^{NH_3}, P_P{}^{NH_3}$ is partial pressure difference of ammonia in reaction channel and permeate channel, respectively.

In the base scenario of the unit cell model, the sweep gas is introduced in a counter-current mode at a temperature of 573K and a pressure of 50 bar. The space velocity, which is a measure of the flow rate of the gas per unit mass of catalyst per unit time, is set at 1.5 $\times$ 10^3 m^3 kg_{cat}^{-1} s^{-1}. The default inlet molar flow rate of the sweep gas is ten times that of the reaction mixture. The counter-current flow configuration for the sweep gas is deliberately chosen due to its demonstrated advantages in improving reactor performance over a co-current flow arrangement under equivalent conditions.

The non-linear set of partial differential equations is solved using the finite volume technique within the ANSYS platform (v. 19.2). Membrane model is adapted from Ji, Wang, Hooman, Bhatia, Diniz da Costa [39] constructed by considering a wall with zero thickness between cooling and reactive stream channels of the micro–HEx unit. This wall causes discontinuity in the fluid transport and prevents modeling of mass transfer of permeable species by Navier–Stokes equations. The pertinent model, however, can be built by implementing source terms on mesh cells that are neighboring the wall. This is realized by a user defined function (UDF), prepared at ANSYS (v. 19.2) platform, for the computation of the source terms (in kg m^{-3} s^{-1}). The source term is computed by taking the edge length of a mesh cell and molar weight of the species into account. Its value is stored in the user defined memory (UDM). Numerical value of UDM is multiplied with –1 and then defined as the source term on the neighboring mesh cell. Source terms are only valid in cells that are within the first rows of mesh cells neighboring the wall (source zone in cooling channel and sink zone in the reactive stream channel). If the source terms are not assigned to any zone, permeation is ruled out and the resulting situation refers to the membraneless case.

In the model, both the reactive mixture and the sweep gas are treated as Newtonian fluids that adhere to the ideal gas law. Additionally, these fluids are considered incompressible, given the negligible frictional pressure loss (<~1%) along the channels. The assumptions of ideal gas behavior and incompressibility are supported by the work of Kucuk, Koybasi and Avci [40]. The solution domain is discretized with the finest mesh configuration supported by the software, consisting of 5.76×10^5 square cells, each with an edge length of 1.25×10^{-5} m.

The second configuration incorporates NH_3 permselective membranes that separate the reaction and permeate channels, with a particular emphasis on NH_3 selectivity (which is 35 and 12 relative to N_2 and H_2, respectively) and permeance (1727 GPU) [27]. Although ZIF-21 membranes show high NH_3 selectivity and permeance, their stability and effectiveness under NH_3 synthesis conditions (above 573K) are not well-understood, leading to their omission from the current study. Laciak, Pez and Burban investigated

NH_3 separation using a zirconia-supported $ZnCl_2$ IMS membrane at 550-600 K, achieving NH_3/N_2 and NH_3/H_2 selectivities greater than 3×10^3 and 1×10^3, respectively, with NH_3 permeability ranging between 2.2 and 7×10^5 barrer. This membrane has shown superior selectivity and stability up to 623K [31]. Consequently, the zirconia-supported $ZnCl_2$ IMS is considered the membrane of choice for selectively removing NH_3 from the reaction channels and allowing it to pass into the permeate channels, as depicted in Figure 3.2b. Given the potential constraints imposed by high temperatures (up to 623K) and the varied composition of the reaction mixture, the NH_3 permeability is set at approximately 160 GPU for a membrane thickness of 3.8×10^{-3} m. The membrane's operation is integrated with the ANSYS platform through user-defined functions (UDF). This mathematical model is employed to examine the influence of operating parameters and in-situ NH_3 withdrawal on heat exchanger performance by adjusting a specific operating parameter within its range while maintaining others at their default values. The results are compared with scenarios in which membrane operation is deactivated by simulating an impermeable wall between the channels. In this setup, the membrane layer is replaced with stainless-steel micro-Heat Exchanger material, enabling only heat transfer, while the sweep gas flow controls the rise in temperature due to the exothermic reaction. Performance is assessed based on the percentage of N_2 conversion, the NH_3 flow rate at the exit of the permeate and reaction channels, and the temperature within the reaction channel. These metrics are derived from the cross-sectional surface-averaged N_2 and NH_3 molar flow rates and temperature measurements. N_2 conversion is calculated as follows

$$N_2\ conversion\ (x_{N_2}, \%) = \frac{F_{N_{2,in}} - F_{N_{2,out}}}{F_{N_{2,in}}} \times 100. \tag{3.7}$$

ANSYS (v. 19.2) is utilized to simulate simultaneous heat transfer and separation processes under laminar flow conditions within micro-Heat Exchanger units, considering both co-current and counter-current flow configurations. The outcomes from ANSYS are compared with those from a MATLAB model, which simulates using a one-dimensional pseudo-homogeneous model. Following the validation of the similarity between the ANSYS and MATLAB models, MATLAB is employed as the integration platform for merging the PBR and micro-Heat Exchanger models beacuse of the simplicity.

After the system is replicated on the ANSYS platform under identical conditions, recovery calculations are performed. In this calculation, recovery, for the same program, indicates how much of the ammonia fed to the reaction channel is drawn into the sweep channel, i.e., how well the membrane performed its function. It is a measure of how much ammonia is extracted. The proximity of this value to 1 indicates that nearly all the fed ammonia passed into the sweep channel. The recovery equation is provided in Equation (3.8) as

$$recovery = \frac{F_{out}^{P}}{F_{in}^{R}} \tag{3.8}$$

where F_{out}^{P} is flow rate of ammonia at the outlet of the permeate channel and F_{in}^{R} is flow rate of ammonia at the inlet of the reaction channel.

Upon conducting recovery calculations and evaluating the outlet temperatures of the sweep and reaction channels, the similarity between the outputs of the MATLAB and ANSYS platforms is scrutinized. Notably, a striking resemblance of 99% is noted between the results obtained from both systems when operating with a 10-fold sweep flow ratio. This comparison of the two models can be found in Table 3.6.

Table 3.6. Recovery calculations for co-current flow in MATLAB and ANSYS.

	$F_{NH_3}^{rxn}$	$F_{NH_3}^{sweep}$	Temperature (K)		Recovery
MATLAB					
Inlet	3.04×10^{-7}	0	623	578	0.91
Outlet	2.70×10^{-8}	2.77×10^{-7}	577.5	577.5	
ANSYS					
Inlet	2.98×10^{-7}	3.67×10^{-11}	621.9	573.2	0.90
Outlet	3.77×10^{-8}	2.68×10^{-7}	577.6	577.6	

The comparisons illustrate a high degree of similarity in results between both models. Consequently, considering capacity for swift parameter adjustments, streamlined testing processes, flexibility in modeling intricate simulations, rapid result generation, and user-friendly interface of MATLAB, it was chosen over ANSYS for this study. Hence, MATLAB is the platform of choice for conducting the research.

4. RESULTS

4.1. Effect of Inlet Temperature

Choosing the appropriate operating temperature for both the Packed Bed Reactor (PBR) and the Microchannel Membrane Heat Exchanger (micro-HEx) is crucial. This choice has a profound effect on the efficiency of the reaction and the lifespan of the membrane. The optimal temperature must strike a fine balance: it should be high enough to accelerate reaction rates but low enough to preserve the durability of membrane. Achieving this balance is vital for maximizing the overall performance of the system. Figure 4.1 illustrates a temperature profile with various inlet temperature ranges for the PBR in a co-current flow setup, with all other parameters set to their default values. It is observed that if the inlet temperature exceeds 573K, the outlet temperature significantly surpasses the tolerance limit of the membrane which is 623K. Therefore, a feed temperature of 573K has been determined to be optimal to ensure the membrane remains within its specified tolerance limits.

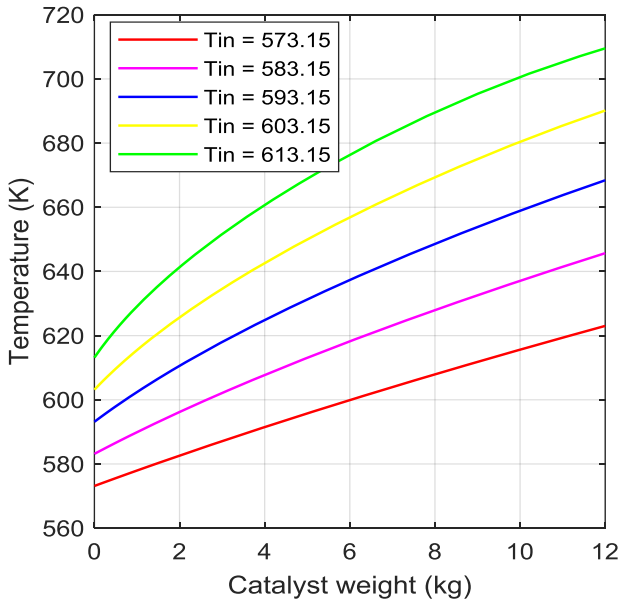

Figure 4.1. Effect of different inlet temperatures.

4.2. Effect of Flow Mode

The effect of flow mode within micro-HEx units on reactor performance is analyzed by switching from co-current to counter-current mode while keeping all other parameters at their default settings. Additional simulations are conducted with the membrane function deactivated to gain a deeper understanding of the benefits of NH_3 separation. Figure 4.2 provides a comprehensive comparison between these configurations, showing temperature and cumulative conversion graphs for a system composed of 9 PBRs and 8 micro-HExs in both co-current and counter-current flow modes. Operating the system in co-current mode causes a significant temperature increase, reaching approximately 175K above the maximum tolerance limit of $ZnCl_2$-IMS membrane which is 623K, ultimately peaking at 800K, also under these conditions, approximately 56% of the cumulative N_2 conversion is achieved, as illustrated in Figure 4.2a and b.

Similar trends are observed in counter-current flow, where improved temperature regulation is evident. In this mode, the maximum temperature exceeds the tolerance by approximately 35K in the case of 9 PBRs. Despite these temperature differences, cumulative N_2 conversion still reaches 56%, similar to the results in co-current flow, as shown in Figure 4.2c and d.

In co-current mode, gases in the sweep channel flow in the same direction as those in the reaction channel. This setup causes rapid temperature changes from the inlet materials to propagate along the reaction channel, often making it difficult to maintain a consistent temperature profile. Conversely, in counter-current mode, the flow in the reaction channel moves in the opposite direction to that in the sweep channel. Here, products exiting the outlet pass through cooler regions, while inlet materials enter the reaction channel at higher temperatures. This configuration allows for better temperature control, as it helps prevent exceeding the maximum temperature limit of the membrane. Additionally, counter-current flow promotes a more balanced reaction by ensuring a more uniform temperature distribution.

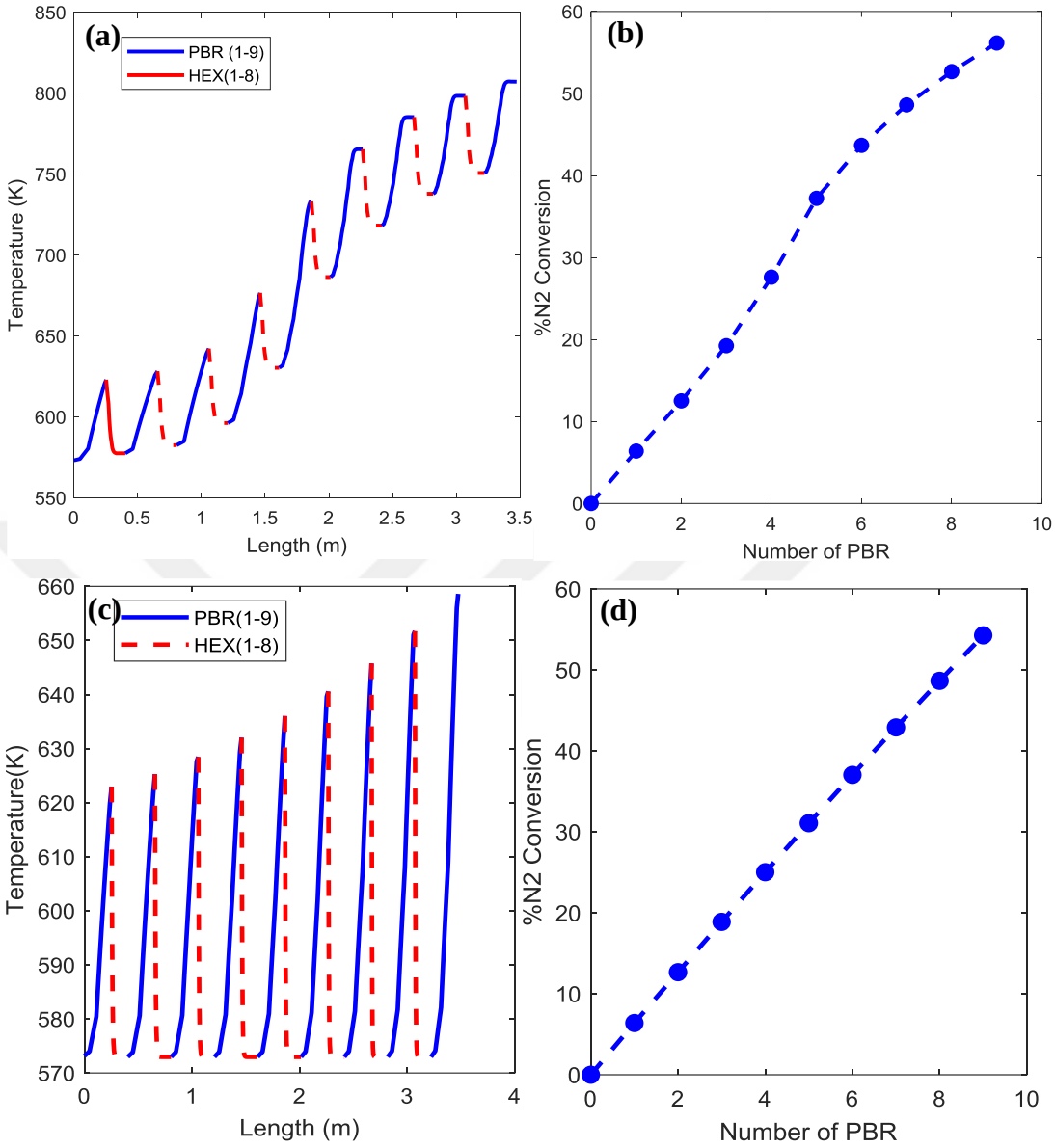

Figure 4.2. Temperature profile and cumulative conversion in (a,b) co-current mode and (c,d) counter-current mode of the system consisting of 9 PBRs and 8 micro-HExs, 573K, 50 bar.

4.3.Effect of Membrane

The information provided underscores the crucial role of membrane activity in controlling temperature and enhancing N_2 conversion during the ammonia synthesis process. As shown in Figure 4.3a, in the counter-current system with an active membrane, the temperature starts to rise after NH_3 is withdrawn following the second PBR, or after the first micro-HEx. Under identical conditions with an inactive membrane, the exit temperature of the second PBR drops to around 585K. This trend persists through subsequent units, with a linear temperature increase observed when the membrane is active, signifying precise system control. Without the membrane, the system experiences a significant temperature drop before stabilizing around the coolant temperature of 573K, demonstrating the effectiveness of membrane.

When the membrane is active, cumulative N_2 conversion increases linearly to 56%, as can be seen in Figure 4.3b. In contrast, without the membrane, the conversion rate increase slows, reaching only 13%. This is because amonnia is not removed from the reaction environment, preventing reaction from progressing. The impact of the membrane on the temperature of subsequent PBRs, and thus on the reaction rate and N_2 conversion, is evident. Modeling highlights the significant role of membrane in temperature control within the ammonia synthesis process. The membrane selectively allows NH_3 gas to pass, enabling its separation from N_2 and H_2 gases. With an active membrane, reaction temperature is better regulated, leading to higher N_2 conversion. This, in turn, enhances ammonia production efficiency and product quality.

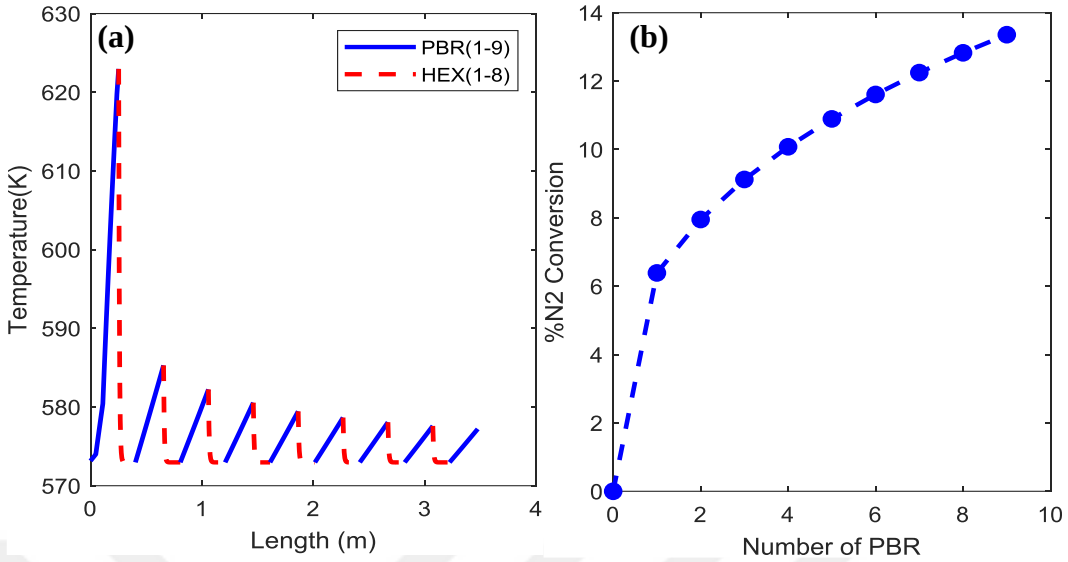

Figure 4.3. (a) Temperature profile (b) cumulative conversion in counter-current mode without membrane of the system consisting of 9 PBRs and 8 micro-HExs, 573K, 50 bar.

4.4.Effect of Additional Fresh Nitrogen Feed

In the first configuration, the output from each PBR directly feeds the reaction channels of serially connected micro-HExs. To explore an alternative approach, the effect of adding fresh N_2 feed at 573K before each PBR is investigated, while keeping the total feed flow constant at 3.33 mol s^{-1}, as can be seen in Figure 4.4. This additional N_2 feed, introduced at the output of each micro-HEx unit, can significantly impact the N_2 conversion, potentially altering the reaction equilibrium and the final product composition.

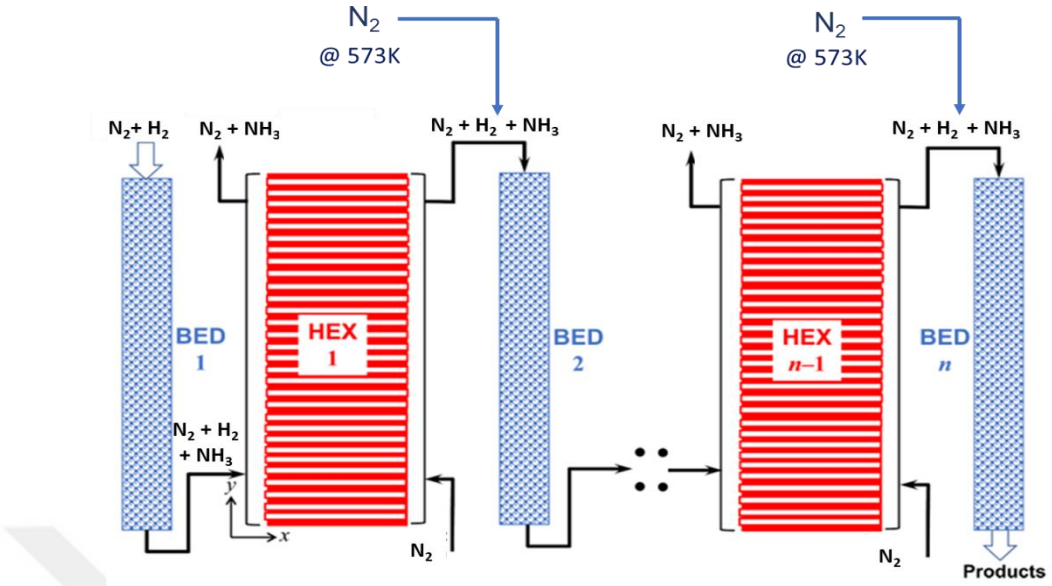

Figure 4.4. Enhanced system configuration featuring additional N_2 supply.

This study reveals distinct temperature profiles when comparing systems with and without the fresh N_2 feed under the same operational conditions. The standard setup shows a gradual temperature rise, peaking around 660K after the 9th PBR, as shown in Figure 4.5a. In contrast, the system with fresh N_2 feed peaks at 632K by the 4th PBR, then gradually decreases to 615K through the 9 PBR setup.

The introduction of fresh N_2 feed significantly affects the converted N_2 amount, as seen in Figure 4.5b. In the standard setup, the converted N_2 amount shows a slight decline. Conversely, with fresh N_2 feed, the converted N_2 amount increases up to the 4th and 5th units, before decreasing after reaching a maximum. The fresh N_2 acts as a coolant, helping to reduce the temperature of the outgoing stream from the reactor and enhancing the cooling effect of the micro-HEx units. Furthermore, the increase in N_2 concentration boosts the reaction rate, thereby increasing the converted N_2 amount.

The findings highlight that introducing fresh N_2 feed before each PBR not only helps in better temperature regulation compared to the base case but also improves N_2 conversion, leading to higher ammonia production. Additionally, the temperature and N_2

conversion peaks at specific points provide critical insights for optimizing the system configuration in future sections.

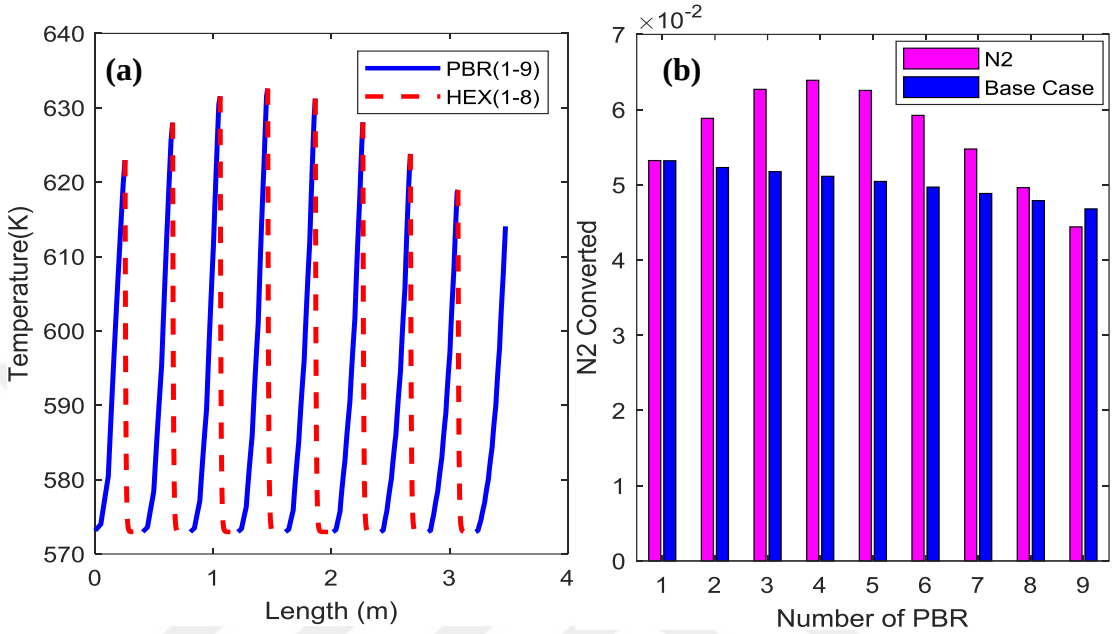

Figure 4.5. (a) Temperature profile (b) amount of converted nitrogen in counter-current mode with membrane and additional nitrogen feed of the system consisting of 9 PBRs and 8 micro-HEXs, 573K, 50 bar.

4.5. Effect of Interconnecting Outlet of Micro-HExs

In the first scenario, cooling is accomplished by introducing nitrogen, freshly supplied at 573K, into the sweep channel of each micro-HEx unit. This section investigates the effects of redirecting the nitrogen from the sweep channel of a micro-HEx unit, combined with the ammonia extracted by the membrane, into the sweep channel of the subsequent unit. This configuration can be seen in Figure 4.6. This strategy addresses the issue of continuously providing fresh nitrogen to the system while enhancing efficiency by recycling the incoming and outgoing streams within the system.

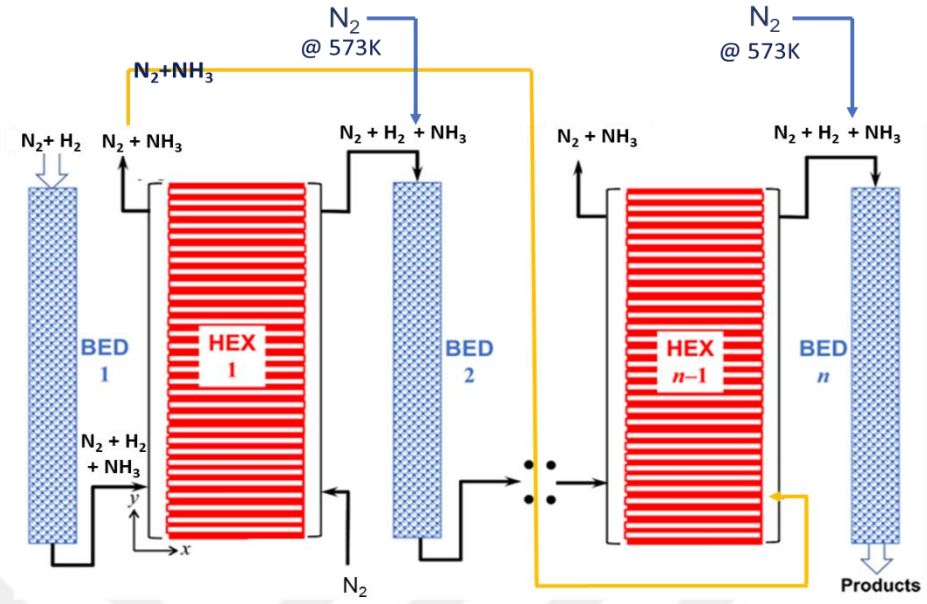

Figure 4.6. System configuration illustrating the interconnected output of the micro-HEx.

A comparison of the performance of heat exchanger between the counter-current (base case) and the counter-current flow mode with a fresh nitrogen supply (second case), as discussed in Section 4.4, with interconnected heat exchanger outputs, is shown in Figure 4.7. According to Figure 4.7a connecting the sweep channels of the micro-HEx units with a single stream under counter-current conditions leads to a variation in the final temperatures, reaching 680K and 660K, compared to the scenario without connection, while following a similar pattern. In the scenario with connected channels, the outlet temperatures of the micro-HEx units are kept at 573K, whereas in the unconnected scenario, they increase gradually, leading to a higher final temperature in the PBR. With a continuous supply of fresh nitrogen, temperature regulation is maintained at around 630K, as shown in Figure 4.7b. The highest temperature is recorded at the 4^{th} and 5^{th} PBRs (634K), eventually stabilizing at 628K. An assessment of setups with additional nitrogen supply, considering both connected and unconnected micro-HEx units, shows similar temperature progression trends, ending with comparable temperature values. In the unconnected case, the temperature reaches 615K at the end of the 9^{th} PBR, while in the connected case, it reaches 628K. It is important to note that in the unconnected scenario, the outlet temperatures of the micro-HEx units stay constant at 573K, in contrast

to the gradual rise observed in the connected scenario. Figure 4.7c illustrating the amounts of nitrogen converted in the different scenarios exhibits a consistent trend across all scenarios, with the setup receiving fresh nitrogen showing fluctuations in the conversion levels of nitrogen, peaking at $6x10^{-2}$ mol s^{-1}, losing its advantage after the 5^{th} PBR, and ending with a final value of $3x10^{-2}$ mol s^{-1}.

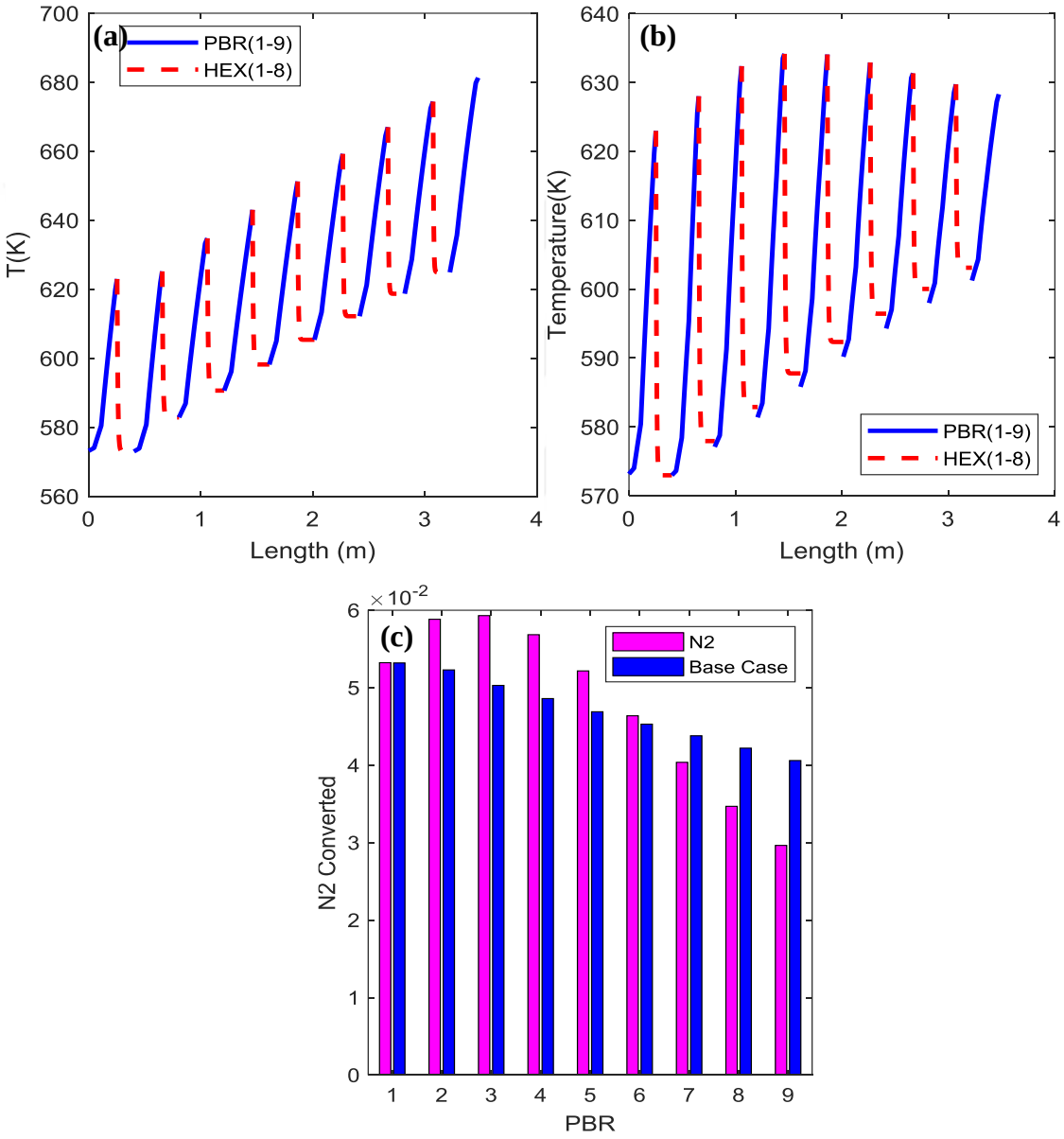

Figure 4.7. Temperature profile with integrating micro-HExs of (a) the base case (b) the case with fresh nitrogen feed (c) amount of nitrogen converted for both cases, 573K, 50 bar.

4.6. Productivity and Number of PBRs

Efficiency in ammonia production is critically dependent on the ratio of produced ammonia to the amount of catalyst used. Increasing ammonia production without a corresponding increase in catalyst usage enhances process efficiency. Optimizing conditions and adopting new technologies can further improve efficiency, allowing for higher ammonia production with reduced catalyst requirements. This not only reduces costs but also promotes sustainability by minimizing environmental impact. Comparing the base case with system efficiencies resulting from previous modifications provides a thorough examination of system efficiency. This analysis helps understand how changes affect efficiency, aiding in the selection of the most optimal system configuration. Productivity is calculated as

$$productivity = \frac{total\ ammonia\ produced}{W_{cat}}. \quad (4.1)$$

The amount of ammonia produced in the base case and N_2 supplied case is calculated as follows:

$$total\ ammonia\ produced = exit\ of\ the\ 5^{th}\ PBR + exit\ of\ the\ 4\ HExs. \quad (4.2)$$

The amount of ammonia produced when micro-HExs are interconnected together is calculated as follows:

$$total\ ammonia\ produced = exit\ of\ the\ 5\ ^{th}PBR + exit\ of\ the\ 4\ ^{th}HEx. \quad (4.3)$$

In Figure 4.8, a detailed comparison is presented regarding the productivity levels achieved in various setups: the base case operating in counter-current flow mode, the scenario involving the introduction of fresh N_2 flow, and the configuration where heat exchangers are interconnected. In Figure 4.8a upon examining the base case, it becomes evident that the productivity values achieved with an increasing number of PBRs range from 0.84 to 0.89x10^{-2} mol s^{-1} kg_{cat}^{-1}, showing a decline. In contrast, when fresh nitrogen feed is introduced into each micro-Heat Exchanger at 573K, as shown in Figure 4.8b, there is a noticeable peak in productivity, reaching 1x10^{-2} mol s^{-1} kg_{cat}^{-1} at the 5^{th} PBR. This marks a 16% improvement over the base case productivity level of 0.86x10^{-2}mol s^{-1}

kg_{cat}^{-1}. The subsequent decrease in productivity suggests an optimal outcome with 5 PBRs.

Another comparison scenario examines a setup where the output of one heat exchanger sweep channel is directed into the input of the subsequent heat exchanger sweep channel. Analysis of the data in Figure 4.8a and b initially indicates that when comparing two base cases, the productivity levels in the second system fluctuate between 0.78 and $0.89x10^{-2}$ mol s^{-1} kg_{cat}^{-1}, showing no significant deviation from the results of the first system. In this context, interconnecting the outputs of heat exchangers in a system operating in counter-current mode does not significantly alter the outcome. However, this configuration proves to be more convenient, accessible, and cost-effective than individually supplying fresh N_2 to sweep channel of each heat exchanger. Also, instead of supplying a fresh N_2 stream, recycling the same stream increases the fraction of ammonia within the sweep channel, which is a significant modification to obtain pure ammonia at a later stage.

Another point of comparison considers the introduction of fresh N_2 to the PBRs. Figure 4.8b reveals a distinct pattern with more pronounced variations in values and a decline observed after the 4^{th} and 5^{th} PBRs. The peak productivity value reaches $0.95x10^{-2}$ mol s^{-1} kg_{cat}^{-1}. Consequently, it is evident that the difference is minimal when compared to the scenario without interconnected micro-HEx units (5%), it can be considered as they are same.

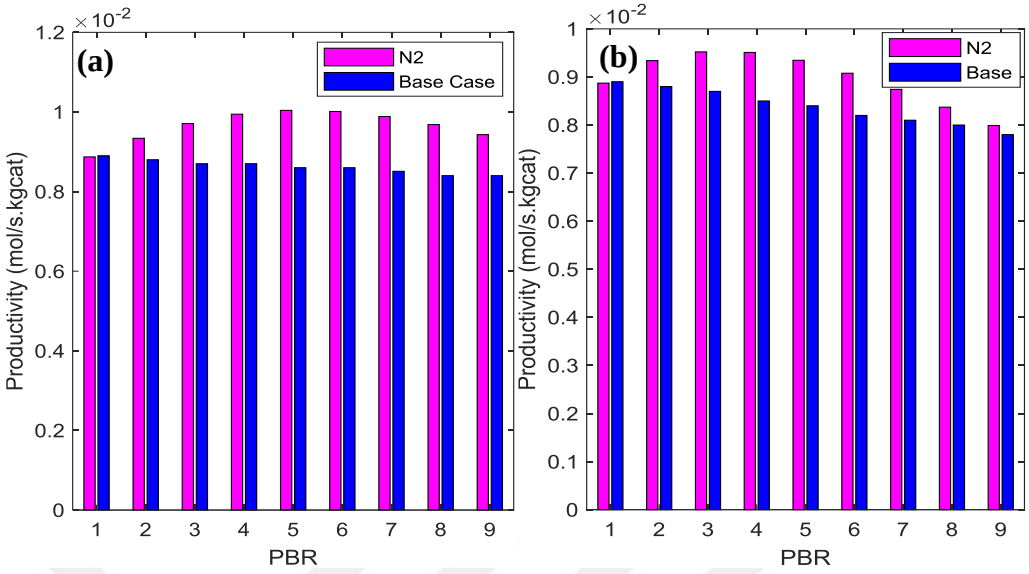

Figure 4.8. Productivity comparisons of (a) without interconnecting micro-HExs (b) with interconnecting micro-HExs, 573K, 50 bar

Drawing from these investigations and results, it is concluded that the configuration comprising 5 PBRs and 4 micro-HEx units operating in counter-current mode, with an additional fresh nitrogen supply to each PBR and interconnected heat exchangers, achieves the highest level of productivity. 5 units are selected to avoid potential issues such as equipment failures. This setup not only demonstrates significant N_2 conversion but also excels in maintaining precise temperature control. A visual representation of this optimal configuration is provided in Figure 4.9.

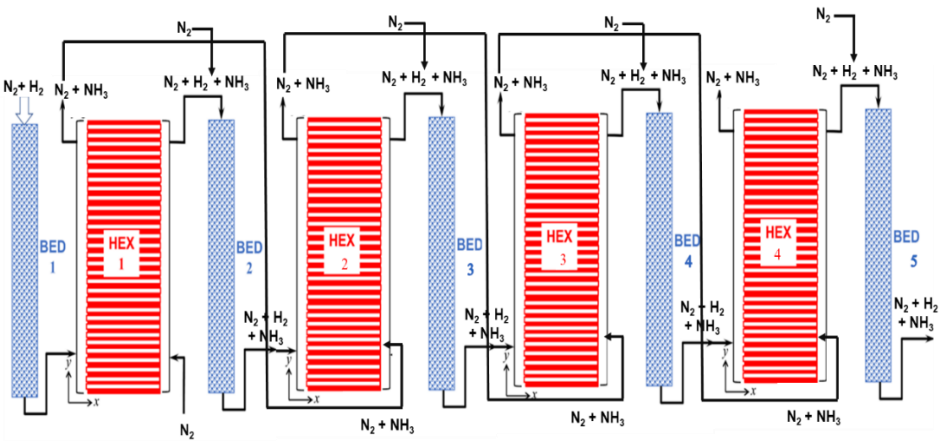

Figure 4.9. Optimal system configuration consisting of 5 units, counter-current mode, additional N_2 supply and interconnetced micro-HExs.

4.7. Separation of Ammonia

As previously noted, in the sweep channel where ammonia passes through a membrane, it combines with flowing nitrogen. The challenge lies in separating these components within the micro-Heat Exchanger sweep channel to separate ammonia, especially in industrial applications requiring ammonia concentrations above specific thresholds. Advanced technologies have been developed for this purpose, featuring sensors that detect ammonia levels and processing units designed for effective separation processes.

One such technology is membrane separation, which selectively allows gases to permeate based on their molecular properties, effectively separating low concentrations of ammonia from nitrogen gas. Another method involves adsorption or absorption techniques, where ammonia concentrations exceeding a certain threshold can be adsorbed and separated using appropriate adsorbents or solvents.

These technologies facilitate the separation of ammonia and nitrogen gas at desired concentrations in industrial settings, thereby improving overall process efficiency. However, selecting the most suitable technology involves evaluating factors like feasibility, cost-effectiveness, and performance.

The study conducted by Padinjarekutt, Li, Ren, Ramesh, Zhou, Li, Belfort, & Yu [41] underscores that maintaining ammonia levels above 2% is sufficient for effective post ammonia separation using these membranes. In scenarios where heat exchangers are interconnected and fresh N_2 is supplied, the NH_3/N_2 ratio in the sweep channel of the entire system is 2.33%.

5. CONCLUSION

The integrated system utilizes packed-bed reactors (PBRs) and microchannel membrane heat exchangers (micro-HExs) under 2D and 1D, non-isothermal, steady-state conditions, modeled using ANSYS and MATLAB. Adiabatic reactions on iron-based catalysts within the PBRs are maintained below 623K to preserve membrane. The system is fed with a mixture at 573K and 50 bar, flowing at 3.33 mol s^{-1} with an H_2/N_2 ratio of 3. The effluent, containing an H_2-N_2-NH_3 mixture, moves through the reaction channels, while nitrogen gas in the sweep channel helps regulate temperature. After membrane separation and cooling, the output is fed into subsequent PBRs for further ammonia synthesis.

Selecting the optimal operating temperature for the PBR and micro-HEx is essential, as it significantly influences both reaction efficiency and membrane longevity. The ideal temperature must enhance reaction rates without compromising the durability of membrane. Observations show that when the inlet temperature exceeds 573K, the outlet temperature surpasses the tolerance threshold of membrane which is 623K. Therefore, maintaining a feed temperature of 573K is crucial to ensure membrane stability.

The study examines the impact of different flow modes in micro-HEx units on reactor performance, transitioning from co-current to counter-current flow. In co-current flow, significant temperature increases exceed membrane tolerance, reaching 800K, with approximately 56% N_2 conversion. Conversely, counter-current flow improves temperature regulation, with a rise of around 35 K, and achieves similar N_2 conversion rates.

Membrane activity plays a vital role in temperature regulation and N_2 conversion in ammonia synthesis. With an active membrane in counter-current mode, precise temperature control results in a linear temperature increase across units. Without

membrane activity, the system stabilizes near the coolant temperature of 573K and nitrogen conversion reaches 13%. The presence of the membrane leads to a linear cumulative N_2 conversion of 56%, underscoring its importance in enhancing reaction rates. Selective NH_3 gas separation by the membrane aids in better temperature control, subsequently increasing N_2 conversion and ammonia production efficiency.

Introducing a fresh N_2 feed at 573K before each PBR has a significant impact on N_2 conversion and product composition. This adjustment affects the reaction equilibrium, leading to distinct temperature profiles within the system. Fresh N_2 acts as a coolant, assisting in temperature control and enhancing the N_2 conversion rate. The results show improved temperature maintenance and increased N_2 conversion, ultimately enhancing ammonia production efficiency.

The study also explores redirecting N_2 flow along with extracted NH_3 from one micro-HEx unit to the next, improving system efficiency. Comparing counter-current and fresh N_2-fed models, temperature stability around 630K is observed with fresh N_2, peaking at the 4^{th} and 5^{th} PBRs. Converted N_2 quantities vary, peaking at 0.95×10^{-2} mol s^{-1}, then declining post 5^{th} PBR to around 0.8×10^{-2} mol s^{-1}.

Ammonia production efficiency depends on maximizing output with minimal catalyst usage. Integrating fresh N_2 increases productivity by 16% at the 5^{th} PBR compared to other setups. The optimal configuration involves 5 PBRs and 4 micro-HExs, in counter-current mode, additional N_2 flow, and interconnected heat exchangers, ensuring high amount of nitrogen converted, productivity and precise temperature control.

Specialized technologies like membranes and adsorption/absorption methods are crucial for separating low-concentration ammonia from nitrogen gas in industrial applications. The study highlights that maintaining ammonia levels above 2% is sufficient for optimal separation efficiency, and the fraction is 2.33% in the best case.

REFERENCES

1. Olabi, A. G., M. A. Abdelkareem, M. Al-Murisi, N. Shehata, A. H. Alami, A. Radwan, T. Wilberforce, K.J. Chae, E.T, Sayed, "Recent progress in Green Ammonia: Production, Applications, Assessment; Barriers, and Its Role in Achieving the Sustainable Development Goals", *Energy Conversion and Management*, Vol. 277, No. 116594, 2023.

2. El-Shafie, M., and S. Kambara, "Recent Advances in Ammonia Synthesis Technologies: Toward Future Zero Carbon Emissions", International Journal of Hydrogen Energy, Vol. 48, No.30, pp. 11237–11273, 2023.

3. Ge, L., B. Zhang, W. Huang, Y. Li, L. Hou, J. Xiao, Z. Mao, and X. Li, "A Review of Hydrogen Generation, Storage, and Applications in Power System", *Journal of Energy Storage*, Vol. 75, No. 109307, 2024.

4. Birol, F., International Energy Agency (IEA), "Key World Energy Statistics", 2021, https://iea.blob.core.windows.net/assets/52f66a88-0b63-4ad2-94a5-29d36e864b82/KeyWorldEnergyStatistics2021.pdf, accessed on June 1, 2024.

5. Shen, H., C. Choi, J. Masa, X. Li, J. Qiu, Y. Jung, and Z. Sun, "Electrochemical Ammonia Synthesis: Mechanistic Understanding and Catalyst Design", *Chem*, Vol. 7, No.7, pp. 1708-1754, 2021.

6. El-Shafie, M., S. Kambara, S. P. Katikaneni, S. N. Paglieri and K. Lee, "Techno-Economic Study And Process Simulation for A Small-Scale Hydrogen Production Plant Based On Ammonia Decomposition", *International Journal of Hydrogen Energy*, Vol. 65, pp. 126–141, 2024.

7. El-Shafie, M., "A Comprehensive Assessment Of Ammonia Synthesis Reaction Kinetics and Rate Equations", *International Journal of Hydrogen Energy*, Vol. 48, No. 92, pp. 35938–35952, 2023.
8. Humphreys, J., R. Lan, and S. Tao, "Development and Recent Pprogress on Ammonia Synthesis Catalysts for Haber–Bosch Process", *Advanced Energy and Sustainability Research*, Vol. 2, No. 1, 2020.
9. Spatolisano, E., and L. A. Pellegrini, "Haber-Bosch Process Intensification: A First Step Towards Small-Scale Distributed Ammonia Production", *Chemical Engineering Research and Design*, Vol. 195, pp. 651–661, 2023.
10. Rouwenhorst, K. H., Y. Engelmann, K. van 't Veer, R. S. Postma, A. Bogaerts, and L. Lefferts, "Plasma-Driven Catalysis: Green Ammonia Synthesis with Intermittent Electricity", Green Chemistry, Vol. 22, No. 19, pp. 6258–6287, 2020.
11. Czekajło, Ł., and Z. Lendzion-Bieluń, "Wustite Based Iron-Cobalt Catalyst for Ammonia Synthesis", *Catalysis Today*, Vol. 286, pp. 114–117, 2017.
12. Gao, W., J. Guo, P. Wang, Q. Wang, F. Chang, Q. Pei, W. Zhang, L. Liu, and P. Chen, "Production of ammonia via a chemical looping process based on metal imides as nitrogen carriers", *Nature Energy*, Vol. 3, No.12, pp. 1067–1075, 2018.
13. https://www.topsoe.com/our-resources/knowledge/our-products/catalysts/km1, accessed on June 1, 2024.
14. Niwa, Y., and K. Aika, "The Effect of Lanthanide Oxides as a Support for Ruthenium Catalysts in Ammonia Synthesis", *Journal of Catalysis*, Vol. 162, No. 1, pp. 138–142, 1996.

15. Bielawa, H., O. Hinrichsen, A. Birkner, and M. Muhler, "The Ammonia-Synthesis Catalyst of the Next Generation: Barium-Promoted Oxide-Supported Ruthenium" *Angewandte Chemie International Edition*, Vol 40, No. 6, pp. 1061–1063, 2001.

16. Narasimharao, K., P. Seetharamulu, K. S. Rama Rao, and S. N. Basahel, "Carbon Covered Mg–Al Hydrotalcite Supported Nanosized RU Catalysts for Ammonia Synthesis", *Journal of Molecular Catalysis A: Chemical*, Vol. 411, pp. 157–166, 2016.

17. Kobayashi, Y., Y. Tang, T. Kageyama, H. Yamashita, N. Masuda, S. Hosokawa, and H. Kageyama, "Titanium-Based Hydrides as Heterogeneous Catalysts for Ammonia Synthesis", *Journal of the American Chemical Society*, Vol. 139, No. 50, pp. 18240–18246, 2017.

18. Hattori, M., T. Mori, T. Arai, Y. Inoue, M. Sasase, T. Tada, M. Kitano, T. Yokoyama, M. Hara, and H. Hosono, "Enhanced Catalytic Ammonia Synthesis with Transformed BaO", *ACS Catalysis*, Vol. 8, No. 12, pp. 10977–10984, 2018.

19. Hattori, M., S. Iijima, T. Nakao, H. Hosono, and M. Hara, "Solid Solution for Catalytic Ammonia Synthesis from Nitrogen and Hydrogen Gases at 50 °C", *Nature Communications*, Vol. 11, No. 1, 2020.

20. Inoue, Y., M. Kitano, S.W. Kim, T. Yokoyama, M. Hara, and H. Hosono, "Highly Dispersed Ru on Electride $[Ca_{24}Al_{28}O_{64}]^{4+}(e^{-})_4$ as a Catalyst for Ammonia Synthesis", *ACS Catalysis*, Vol. 2, No. 2, pp. 674–680, 2014.

21. Lu, Y., J. Li, T. Tada, Y. Toda, S. Ueda, T. Yokoyama, M. Kitano, and H. Hosono, "Water Durable Electride Y_5Si_3: Electronic Structure and Catalytic Activity for Ammonia Synthesis", *Journal of the American Chemical Society*, Vol. 138, No. 12, 2016.

22. Jacobsen, C. J., "Novel Class of Ammonia Synthesis Catalysts", *Chemical Communications*, No.12, pp.1057–1058, 2000.

23. Bion, N., F. Can, J. Cook, J. S. J. Hargreaves, A. L. Hector, W. Levason, A. R. McFarlane, M. Richard, and K. Sardar, "The Role of Preparation Route upon the Ambient Pressure Ammonia Synthesis Activity of Ni_2Mo_3N", *Applied Catalysis A: General*, Vol. 504, pp. 44–50, 2015.

24. Kojima, R., and K. I. Aika, "Cobalt Molybdenum Bimetallic Nitride Catalysts for Ammonia Synthesis", *Applied Catalysis. A, General*, Vol. 215, No. 1-2., pp. 149–160, 2001.

25. Cao, H., J.Guo, F. Chang, C. Pistidda, W. Zhou, X. Zhang, A. Santoru, H. Wu, N. Schell, R. Niewa, P. Chen, T. Klassen, and M. Dornheim, "Transition and Alkali Metal Complex Ternary Amides for Ammonia Synthesis and Decomposition", *Chemistry*, Vol. 23, No. 41, pp. 9766–9771, 2017.

26. Ye, T. N., S. W. Park, Y. Lu, J. Li, M. Sasase, M. Kitano, T. Tada, and H. Hosono, "Vacancy-Enabled N_2 Activation for Ammonia Synthesis on an Ni-Loaded Catalyst", *Nature*, Vol. 583, No. 7816, pp. 391–395, 2020.

27. Wei, Q., J. M. Lucero, J. M. Crawford, J. D. Way, C. A. Wolden, and M.A.Carreon, "Ammonia Separation from N_2 and H_2 over LTA Zeolitic Imidazolate Framework Membranes", *Journal of Membrane Science*, Vol. 623, No. 119078, pp.623, 2021.

28. Phillip, W. A., E. Martono, L. Chen, M. A. Hillmyer, and E. L. Cussler, "Seeking an Ammonia Selective Membrane Based on Nanostructured Sulfonated Block Copolymers", *Journal of Membrane Science*, Vol. 337, No.1-2, pp. 39–46, 2009.

29. He, Y., and E. Cussler, "Ammonia Permeabilities of Perfluorosulfonic Membranes in Various Ionic Forms", *Journal of Membrane Science*, Vol. 68, No. 1-2, pp. 43–52, 1992.

30. Bhown, A., and E. L.Cussler, "Mechanism for Selective Ammonia Transport Through Poly (Vinylammonium Thiocyanate) Membranes", *Journal of the American Chemical Society*, Vol. 113, No. 3, pp. 742–749, 1991.

31. Laciak, D.V., G.P. Pez, and P.M. Burban, "Molten Salt Facilitated Transport Membranes. Part 2. Separation of Ammonia from Nitrogen and Hydrogen at High Temperatures", *Journal of Membrane Science*, Vol. 65, No. 1-2, pp. 31–38, 1992.

32. Koybasi, H.H., A.K. Avci, "Numerical analysis of CO_2-to-DME conversion in a membrane microchannel reactor", *Industrial & Engineering Chemistry Research*, Vol. 61, No. 30, pp. 10846-10859, 2022.

33. Avci, A.K., D.L. Trimm, and Z.I. Onsan, "Heterogeneous Reactor Modeling for Simulation of Catalytic Oxidation and Steam Reforming of Methane", *Chemical Engineering Science*, Vol. 56, No. 2, pp. 641-649, 2021.

34. Onsan, Z.I. and A.K. Avci, *Fuel Cells: Technologies for Fuel Processing*, Elsevier Science, Amsterdam, 2011.

35. Hagen, S., R. Barfod, R. Fehrmann, C.J.H. Jacobsen, H.T. Teunissen, I. Chorkendorff "Ammonia Synthesis with Barium-Promoted Iron–Cobalt Alloys Supported on Carbon", *J Catal*, Vol. 214, No.2 , pp. 327–335, 2003.

36. Zhang, Z., J.D. Way, and C.A. Wolden, "Design and Operational Considerations of Catalytic Membrane Reactors for Ammonia Synthesis", *AIChE J*, Vol. 67, No. 8, 2021.

37. Sehested, J., C. J. Jacobsen, E. Törnqvist, S. Rokni, and P.Stoltze, "Ammonia Synthesis over a Multipromoted Iron Catalyst: Extended Set of Activity Measurements, Microkinetic Model, and Hydrogen Inhibition", *Journal of Catalysis*, Vol. 188, No.1, pp. 83–89, 1999.

38. Uriz I., G. Arzamendi, ´E. Lopez, J. Llorca, LM. Gandía, "Computational Fluid Dynamics Simulation of Ethanol Steam Reforming in Catalytic Wall Microchannels", Chem Eng J., Vol. 167, No. 2, pp. 603–609, 2011.

39. Ji G., G. Wang, K. Hooman, S. Bhatia, J.C. Diniz da Costa, "Computational Fluid Dynamics Applied to High Temperature Hydrogen Separation Membranes", *Frontiers of Chemical Science and Engineering*, Vol. 6, No.1 , pp. 3-12, 2012.

40. Kucuk, E., H. H. Koybasi, and A. K. Avci, "Beyond Equilibrium Ammonia Synthesis in a Membrane and Heat Exchange Integrated Microreactor: A Modeling Study", *Fuel*, Vol. 357, No. 129858, 2024.

41. Padinjarekutt, S., H.Li, S. Ren, P. Ramesh, F. Zhou, S. Li, G. Belfort, and M. Yu, "Na+-Gated Nanochannel Membrane for Highly Selective Ammonia (NH_3) Separation in the Haber-Bosch Process", *Chemical Engineering Journal*, Vol. 454, No. 139998, 2023.

APPENDIX A. SUPPORTING INFORMATION

A.1. Pressure Drop

The pressure drops determined using the Ergun Equation in the PBR units are negligible. The visualization of pressure changes is provided in Figure A.1. As can be seen from figures pressure drop for the system is maximum 1.8%.

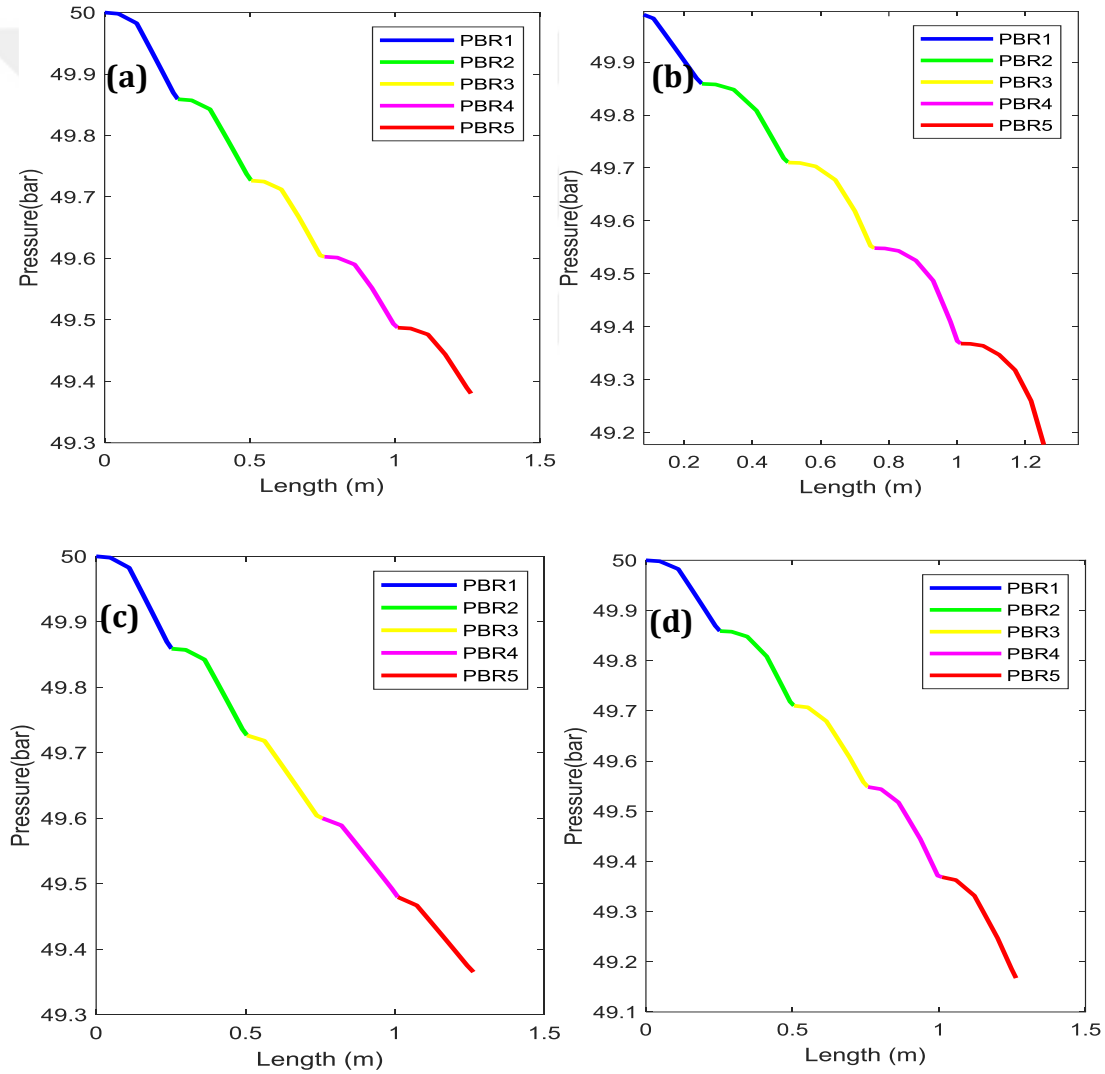

Figure A.1. Pressure drop of case (a) with counter-current, (b) with additional N_2 feed, (c) with interconnected micro-HExs (d) optimum case.

A.2. Property Correlations

The set of correlations and mixing laws in Table A.1 is used to predict the physical properties of fluid mixtures in the gas phase.

Table A.1. Set of correlations and mixing laws

Mixture viscosity	$\mu_m = \sum_{i=1}^{N_g} \frac{y_i \mu_i}{\sum_{j=1}^{N_g} y_j \Phi_{ij}}$
	$\Phi_{ij} = \frac{1}{\sqrt{8}} \left(1 + \frac{M_i}{M_j}\right)^{-1/2} \left[1 + \left(\frac{\mu_i}{\mu_j}\right)^{1/2} \left(\frac{M_j}{M_i}\right)^{1/4}\right]^2$
Mixture thermal conductivity	$k_m = \sum_{i=1}^{N_g} \frac{y_i k_i}{\sum_{j=1}^{N_g} y_j \Phi_{ij}}$
Diffusivity of species i in the mixture	$D_{i,m} = \frac{1 - y_i}{\sum_{j=1}^{N_g} y_i / D_{ij}}, j \neq i$
Binary diffusivity	$D_{ij} = \frac{10^{-3} T^{1.75} \left(\frac{1}{M_i} + \frac{1}{M_j}\right)^{1/2}}{p \left[(\sum \upsilon)_i^{1/3} + (\sum \upsilon)_j^{1/3}\right]^2}$
Mixture heat capacity	$c_{p,m} = \sum_{j=1}^{N_g} c_{p,i} y_i$
Density and molecular weight of the mixture	$\rho_m = \frac{P M_m}{ZRT}, M_m = \sum_{j=1}^{N_g} M_i y_i$